# *Real-time visualization reveals Mycobacterium tuberculosis ESAT-6 disrupts phagosome via fibril-mediated vesiculation*

Debraj Koiri [1,5], Mintu Nandi[2*], Abik Hameem P M[1,5*], Aher Jayesh Bhausaheb[1,5], Geetanjali Meher [1,5], Assirbad Behura[1,5], Akhil Kumar[3], Vineet Choudhary[3], Sandeep Choubey[4,5], Mohammed Saleem[1,5,6]

## Affiliations

[1] School of Biological Sciences, National Institute of Science Education & Research (NISER), Bhubaneshwar, India.
[2] Department of Chemistry, Indian Institute of Engineering Science and Technology, Shibpur, India.
[3] Department of Biotechnology, All India Institute of Medical Sciences, New Delhi, India.
[4] Institute of Mathematical Sciences (IMSc), Chennai, India.
[5] Homi Bhabha National Institute (HBNI), Mumbai, India.
[6] Center for Interdisciplinary Sciences, National Institute of Science Education & Research (NISER), Bhubaneshwar, India.

Correspondence: saleem@niser.ac.in

Classification: Biological Sciences, Biophysics & Computational Biology.

Keywords: Membrane Biophysics, *in vitro* reconstitution, Mycobacteria, Host-pathogen interactions, Membrane fission.

# Abstract

*Mycobacterium tuberculosis (Mtb)* evades host defense by hijacking and rupturing the phagosome, enabling it to escape to the host cytosol for its survival. ESAT-6, a secreted virulence protein of *Mtb*, is known to be critical for phagosome rupture. However, the mechanism of ESAT-6-mediated disruption of the phagosomal membrane remains unknown. Using *in vitro* reconstitution and numerical simulations, we discover that ESAT-6 polymerization remodels and vesiculates phagosomal membrane. In contrast to the pore formation triggered by a bilayer-spanning conformation, we find that the binding of ESAT-6 to the phagosomal membrane is shallow. Such shallow insertion leads to membrane shape transition leading to tubular and bud-like deformations on the membrane in a concentration-dependent manner, facilitated by the reduction in membrane tension and compressibility modulus. Strikingly, our observations suggest that ESAT-6 polymerizes in bulk and on the membrane, both *in vitro* and in macrophage. Numerical simulations demonstrate that growing fibrils generate both radial and tangential forces causing local remodeling and shape transition of the membrane. Using micropipette aspiration, we quantitatively show that ESAT-6 bound tensed membrane undergoes local changes in membrane curvature and lipid phase separation, also facilitated by the direct contact of the bacteria inside the phagosome. Nonetheless, the vesiculation of the buds is primarily driven by the forces exerted by the polymerization of ESAT-6. Such ESAT-6 mediated vesiculation induces apoptosis and host cell death in a concentration and time-dependent manner that promotes infection. Overall, the findings provide mechanistic insights into the long-standing question of phagosome disruption by *Mtb* for its escape.

## Introduction

*Mycobacterium tuberculosis* (*Mtb*), the causative agent of tuberculosis, survives inside the host by regulating the phagosome maturation and rupture to escape into the cytosol of the host cell [1]. ESAT-6 (6kDa early secretory antigen target), a highly immunogenic effector secreted by *Mtb*, has been identified as a critical protein involved in the process of phagosome (also referred to as Mycobacteria closed vacuole) rupture [2]. ESAT-6 is known to be secreted as ESAT-6: CFP-10 heterodimeric complex, stabilized by two-salt bridges. This is crucial for the secretion and the stability of ESAT-6 in the intracellular environment of the phagosomal lumen [3]. Native ESAT-6/CFP-10 heterodimer extracted from *Mycobacterium tuberculosis* was found to dissociate under acidic pH, however, only ESAT-6 but not CFP-10 is known to interact with the phagosome membrane [4]. Purified recombinant ESAT-6 has been implicated in lysis of artificial lipid membranes [4], red blood cells [5] and cultured macrophages through permeabilization of both the phagosome membrane as well as cell membrane upon gaining access to the cytoplasm [6-8]. Purified ESAT-6, but not other ESX-1-secreted proteins, has been shown to induce pore formation in host cell membranes [5, 9, 10]. The membrane-interacting activity of ESAT-6 is known to largely depend on acidic pH-dependent conformational changes in vitro [9]. It has also been reported that many of the pore-forming activities ascribed to ESAT-6 are due to the residual detergent contamination in ESAT-6 purification adopting widely used protocols [11, 12]. ESAT-6 is found to induce significant deformation of nonacidified phagosome. Yet under acidic conditions liposome membrane is known to undergo lysis induced by both the native as well as recombinant ESAT-6 in the absence of contaminating detergents [13].

Interestingly, a recent study reported that ESAT-6 alone is not sufficient for phagosome disruption. Instead the direct bacterial physical contact was found to be important for gross phagosomal membrane disruption [11]. *In vivo* observations also suggest that ESAT-6 required additional factors such as the lipid phthiocerol dimycocerosate for the phagosomal disruption [12, 14, 15]. *Mycobacterium marinum* transposon mutants have also been found to be capable of phagosome damage despite their inability to secrete ESAT-6 hinting that ESAT-6 alone may not be sufficient for the ESX-1 virulence function [16]. However, there is also strong evidence supporting ESAT-6's direct role in phagosome lysis and virulence [9, 17, 18]. Most recently, the C terminus of ESAT-6 was shown to be required for phagosomal membrane damage [13]. Though the ability to damage the phagosomal membrane has emerged as central to *Mtb* virulence, the mechanism of ESAT-6 mediated phagosome membrane disruption remains poorly understood [1]. In particular, the insights on the dynamics of ESAT-6 interaction and membrane remodeling of phagosome are lacking[2].

In this work, we demonstrate that ESAT-6 undergoes fibrillation both *in vitro* and *in* vivo, and subsequently disrupts the phagosome through vesiculation. Our findings

reveal that the binding of recombinant ESAT-6 to the membrane is shallow, penetrating only to C5 of the acyl chain in the interacting leaflet of the bilayer, rather than spanning the entire bilayer as previously believed. We discover that the ESAT-6 leads to the formation of small tubules to spherical buds on the membrane surface in a concentration-dependent manner, accompanied by a reduction in membrane tension and compressibility modulus. However, bud fission occurs only around 24 hours, coinciding with the timescale in which ESAT-6 surprisingly undergoes fibrillation, forming a network of randomly aligned polymers both in vitro and in vivo. Numerical simulations demonstrate that growing fibrils can generate both radial and tangential forces, causing local remodeling and reshaping of the membrane. We quantitatively show that the binding of the lower oligomer of ESAT-6 on a membrane under tension, as a result of forces generated by fibrils, triggers local changes in membrane curvature and lipid phase separation. The lipid phase separation in the phagosome membrane may also be induced by the direct contact associated with the bacterial load. Finally, the vesiculation of the bud takes place by a three-fold increase in the areal strain on the phagosomal membrane that subsequently induces apoptosis and host cell death likely helping in the infection.

# Result

## ESAT-6 penetrates till C5 of the acyl chain and induces tubular deformations in the phagosome membrane mimic

*M. tuberculosis* blocks phagosomal maturation by secreting the virulence effector protein ESAT-6 through the ESX-1 secretion system. ESAT-6 is known to have a membranolytic activity that helps *M. tuberculosis* escape into the cytosol [1, 13]. However, the mechanism of ESAT-6-mediated disruption of the phagosomal membrane remains unknown. The binding affinity of ESAT-6 on phagosomal membrane mimic (40% DOPC, 5.5% DOPE, 22% SM, and 32.5% Chol)[19] was quantified using the tryptophan intrinsic fluorescence of ESAT-6. Upon titration of 5 μM of ESAT-6 with the increasing lipid concentration (ranging from 0 to 600 μM) using liposomes, we observed a concentration-dependent reduction in the fluorescence intensity of ESAT-6 tryptophan residues hinting at weak association with the membrane (i.e, membrane binding affinity, $K_d$ ~ 400μM; (Fig. 1b). This is in line with the recently reported rapid self-association of ESAT-6 as a result of its low dissociation constant (i.e, $K_d$ ~ 1.5μM) [20]. The decrease in fluorescence intensity signifies that the tryptophan residues are interacting or embedded within the hydrophobic environment of the membrane. The maximum tryptophan fluorescence of ESAT-6 was observed between 315 nm to 335 nm (Extended Data Fig. 1).

To visualize the dynamics of ESAT-6 interaction in real-time, we first immobilized giant unilamellar vesicles (GUVs, 10-50μm) mimicking phagosomal composition doped with 0.01% biotinylated-PEG to facilitate conjugation to streptavidin passivated surface. The GUVs were labeled with 0.1% Rhodamine-PE and incubated with 5μM of FITC-labeled recombinant mycobacterial ESAT-6 (*see methods*). Though this is topologically opposite, the micrometer-scale of the phagosome and the cell membrane will both have a zero mean curvature and thus appear planar for ESAT-6 of 10-20 Å width [21]. ESAT-6 homogenously bound to the GUV surface within 10 seconds of protein injection, followed by tubular deformation of the immobilized GUVs within a minute (Fig. 1c and S1- Movie & Extended Data Fig. 2). Though fine tubular structures were observed on the GUV membrane surface upon the injection of ESAT-6, it is difficult to rule out the possibility that the observed structures arise due to the broad point spread function in the confocal imaging (Fig. 1c-d). Visualizing protein-induced small tubular structures, particularly during their emergence, can be challenging as they are mostly below the optical resolution [22, 23]. The super-resolution image of the equatorial plane of the ESAT-6 bound GUV revealed discrete local binding and changes in curvature capturing the onset of membrane shape transition (Fig. 1e). The diffusion of the membrane-bound ESAT-6 was found to only partially decrease as evident from significant fluorescence recovery after photobleaching, and the rate of diffusion was estimated to be 0.11 $\mu m^2$/sec using the Soumpasis equation as described in the method (Fig. 1f). This also supports the observed weak-association of ESAT-6 with the membrane in the monitored time scale. To examine the ESAT-6

insertion in the membrane, we performed the steady-state fluorescence using depth-sensing fluorescence quenching probes 5-Doxyl-PC & 12-Doxyl-PC with a constant concentration of 10 mol%. Depth-sensitive fluorescence quenching allows estimating the depth of membrane penetration of a fluorophore attached to the target molecule with the quenchers attached at various depths of the membrane bilayer [24, 25]. ESAT-6 has three tryptophan residues in its sequence that allowed us to monitor the fluorescence intensity of the tryptophan in the presence of the doxyl probes (Fig. 1g). In contrast to the bilayer spanning model for pore formation [4, 5, 10, 26], we observed that as the concentrations of ESAT-6 increased, the 5-Doxyl-PC that corresponds to a depth ~12 Å from the center of the bilayer, showed more quenching effect compared to the 12-Doxyl-PC. This suggests that ESAT-6 does not penetrate the entire bilayer instead it inserts only till C5 of the acyl chain in the interacting leaflet. We further looked at the lipid specificity of ESAT-6 interaction in the phagosomal lipid environment and found that ESAT-6 has a preferential binding for the phosphatidylcholine (DOPC) head group. Amongst the reconstituted minimal lipid membranes of the phagosome model membrane, the highest binding intensity was observed for the DOPC membrane, followed by the DOPC/Sphingomyelin membrane. The presence of 30% cholesterol in the DOPC membrane results in the weakest binding of ESAT-6 hinting at the possible role of packing densities in the binding of ESAT-6 (Fig. 1h). Though the observed difference in binding intensities of ESAT-6 between individual lipid membranes is quite low, however, the phagosomal membrane showed many folds higher binding (Fig. 1i).

## ESAT-6 binding reduces the membrane tension and makes it more compressible

To understand the observed shape elasticity and deformations in the phagosome model membrane induced by ESAT-6, we first examined the fate of the cell membrane tension upon ESAT-6 binding. As the initial composition of the phagosomal membrane is derived from the cell membrane[27], particularly, the outer leaflet of the cell the membrane being the same as the inner leaflet of the engulfing phagosome. We thus monitored the fluorescence lifetime change in the cell membrane of cultured THP-1 differentiated macrophages treated with ESAT-6 over ten minutes and doped with 100nM of Flipper-TR, a membrane tension sensor, [28, 29]. We found that binding of 5μM ESAT-6 to macrophage cell membrane results in a decrease in the fluorescence lifetime from 4.2 ns to 3.4 ns indicating a significant reduction in the cell membrane tension (Fig. 2a, c). It is reasonable to say that ESAT-6 interaction with the phagosomal membrane would also reduce the membrane tension. Indeed, the fluorescence lifetime of the tension sensor in the reconstituted GUVs mimicking phagosomal membrane decreased from 4.5 ns to 3.7 ns upon the interaction with 5μM ESAT-6 (Fig. 2b, c) suggesting a reduction in the tension. The magnitude of the observed changes is significant as previously reported for endosomes [29].

We next examined the response to compression, in the plane of the membrane, upon the binding of ESAT-6 using lipid monolayer membranes. Langmuir monolayers enable quantification of lateral lipid interactions and compressibility modulus [30-32]. First, the surface activity of ESAT-6 was established through its interfacial behavior at the air/buffer interface in the absence of lipids. The addition of 5 μM ESAT-6 in the buffered sub-phase equilibrated to 0 mN/m led to an increase in the surface pressure to 27 mN/m and stabilized over ~1 hour suggesting the surface active and amphiphilic nature of ESAT-6 (Extended Data Fig. 3). In the presence of phagosomal model lipid monolayer equilibrated at bilayer equivalence pressure of ~31 mN/m (i.e, bilayer equivalence range of 30-35 mN/m), the addition of ESAT-6 led to the rise in surface pressure up to ~33 mN/m over an hour hinting at weak interaction with membrane (Extended Data Fig. 4). We next examined the ESAT-6-induced changes in area per lipid molecule and phase behavior of the phagosomal model monolayer membrane. Analysis of the ESAT-6 bound phagosomal model membrane surface pressure ($\pi$)-area isotherm ($A$) revealed a plateau at 28-32 mN/m suggesting the transition from a liquid-expanded ($l_e$) to a liquid-condensed ($l_c$) phase (Fig. 2d). The compressibility modulus ($C_s^{-1}$) of the ESAT-6 bound membrane was extracted from the $\pi$-$A$ isotherm using the following equation -

$$C_S^{-1} = -A\,(d\pi/dA)_T \qquad (1)$$

The $C_s^{-1}$ of the monolayer at the bilayer equivalent surface pressure of ~ 30-35mN/m is considered to be analogous to the elasticity of a bilayer membrane because the hydrophobic free energy and area per lipid are similar to that in membrane bilayer at this pressure [30, 32, 33]. The $Cs^{-1}$ of the phagosomal membrane decreased two-fold from ~180 mN/m to ~ 90 mN/m upon the interaction of ESAT-6, suggesting the membrane is more compressible and thus, easier to deform (Fig. 2e).

## Higher surface density of ESAT-6 induces phagosomal membrane budding and initiation of vesiculation

*Mycobacterium tuberculosis (Mtb)* relies on the ESX-1 secretion system for the secretion of ESAT-6 inside the phagosome. The physiological concentration of ESAT-6 inside the phagosome remains unknown, however, considering the confined volume of the phagosome, the local concentration of the secreted protein can be high. Thus, we used a range of concentration from 1-20 μM in line with the previous *in vivo* and *in vitro* studies that used concentrations ranging from 1-50 μM[34-36]. Likely, the effective concentration of the protein inside the confined volume of the phagosome will rise over time. Considering the size of phagosome to be in the order of 2-5 μm, the ratio of the available surface area and number of secreted protein molecules inside a confined volume should be very low. We questioned whether the rise in the phagosome membrane-bound surface density of ESAT-6 induces any further remodeling and shape deformation. To capture this in real-time, we incubated 20 μM of unlabeled ESAT-6 with the immobilized phagosomal membrane mimic GUVs

248 labeled with 0.1% Rhodamine-PE. Extrapolating the change in the area per lipid
249 molecule of a monolayer membrane upon the binding of unlabelled ESAT-6 for a GUV
250 surface, the surface density of the ESAT-6 was estimated to be ~ 74 x $10^4$ molecules
251 bound on GUV with a radius of 15 μm. (Extended Data Text). To establish the
252 functional role of ESAT-6 binding, we opted not to use FITC-labelled ESAT-6 at higher
253 concentrations to rule out any potential hindrance caused by the FITC molecule on
254 protein binding. Interestingly, time-lapse imaging revealed that ESAT-6 induces large
255 membrane tubules and buds on the membrane having both positive and negative
256 curvature (Fig. 2g-h and S4-Movie). No such deformations were observed when the
257 membrane was treated with other proteins (i.e., 20 μM CFP-10, BSA) at high
258 concentrations ruling out the role of osmolarity changes as a result of protein flux and
259 proving the specificity of ESAT-6 interaction (Fig. 2f and S2-3 Movie). The equatorial
260 plane of the ESAT-6 bound GUVs showed some seemingly detached free vesicles,
261 however, we think most are still connected with tubular necks that remained out of
262 focus. Occasional vesiculation mediated by ESAT-6 crowding cannot be ruled out as
263 observed in the z-stack and such observation was not common. The buds remained
264 attached even after 45 mins of monitoring without undergoing any visible change (Fig.
265 2i). Size distribution analysis revealed that most of the budded vesicle sizes are less
266 than 3 μm compared to the mother vesicle sizes around 15-20 μm, in diameter
267 (Extended Data Fig. 6). Though the observed size appears to be several folds higher
268 than the intracellular scale, however, we think that the size of the bud might scale with
269 the area available on the mother vesicle and lead to a broad range of bud size as the
270 mother vesicle loses area [37]. We speculate that for a phagosome of size ~2 μm this
271 might result in the formation of phagosome buds much smaller in size often making it
272 challenging to visualize as well as demarcate from other vesicular compartments due
273 to technical limitations.
274
275 Previous reports have shown that Mycobacterial translocation from phagolysosome or
276 phagosome into the cytoplasm, in a non-apoptotic cell, can take upto few hours to
277 days and involves ESAT-6 secretion as well as direct contact of the bacteria[6, 11].
278 We hypothesized that prior to the *Mtb* escape, ESAT-6-mediated remodeling should
279 reflect in the polarity of the phagosomal membrane interface. Fluorescence lifetime is
280 known to be sensitive to the changes in the local environmental polarity of the
281 membrane [38]. We quantified the fluorescence lifetime of the tryptophan residue of
282 ESAT-6, at 30 min and 24 hours post-treatment, by incubating 1 μM, 5 μM, and 10 μM
283 ESAT-6 concentrations with the phagosomal model membrane. The fluorescence
284 lifetime of the tryptophan residue of ESAT-6 decreased around 24 hours, but not at 30
285 min, suggesting an increase in the local polarity over time (Fig. 2j & Extended Data
286 Fig. 5). This decrease in the fluorescence lifetime could be due to the insertion of water
287 molecules into the membrane. However, at higher concentrations of ESAT-6, the
288 change in the fluorescence lifetime is less pronounced due to a relatively greater
289 number of proteins on the membrane which hinders the insertion of water molecules
290 (Fig. 2k). Overall, the observations suggest that though tubulation and budding is a

291 fast process, the local polarity increased only at later time scales of ~ 24 hours till
292 which the predominant number of buds remain undetached.
293

## 294 ESAT-6 fibrillation drives the rate of vesiculation of the phagosomal
295 membrane
296

297 Many of the bacterial secretory proteins have been speculated to possess
298 amyloidogenic propensity[39]. Perplexed by the observation that the buds
299 predominantly remain attached to the phagosomal membrane we next examined
300 ESAT-6 behavior in the presence of a phagosomal membrane interface, for a longer
301 duration of time. Thus, we first investigated whether ESAT-6 shows any fibrillation
302 characteristics estimated through Thioflavin T (ThT) fluorescence assay (Fig. 3a).
303 Surprisingly, we discovered that 20 μM ESAT-6 undergoes rapid fibrillation under the
304 phagosomal acidic pH of ~ 5.5 without any visible nucleation or lag phase and reaches
305 the equilibrium phase around ~24 hours, unlike other fibrillating proteins that take
306 much longer[40, 41] (Fig. 3a). Aggregated ESAT-6 structures were also visualized in
307 solution via microscopy around ~24 hours (Extended Data Fig. 8). On the contrary,
308 the presence of the phagosomal membrane interface leads to a significant slowdown
309 of the ESAT-6 fibrillation kinetics as evident from the nucleation phase lasting around
310 ~20 hours. Subsequently, fibrillation began around ~20 hours and reached the
311 equilibrium by ~35 hours (Fig. 3a). Certain lipids have been found to inhibit or retard
312 the fibrillation kinetics of several amyloidogenic proteins [42] that might explain the
313 observed slowdown in fibrillation kinetics. Further, no fibrillation of CFP-10 was
314 observed in solution or in the presence of membrane confirming the specificity of
315 ESAT-6 fibrillation (Extended Data Fig. 7). The fibrillation behavior of ESAT-6 led us
316 to test whether the same can happen inside THP1-derived macrophages under
317 cellular environment. Indeed, upon incubating recombinant FITC labeled ESAT-6 with
318 THP-1 derived macrophage treated with a NIT-OH (a red fluorescent dye specific for
319 cell membrane), the ESAT-6 is phagocytosed (Fig. 3b). Further, the phagocytosed
320 ESAT-6 vesicles pinch off from the cell membrane and the ESAT-6 intensity inside the
321 phagosome is found increase by 8-fold compared to the extracellular environment
322 (Fig. 3c). Such puncta are often related to the aggregated forms of the proteins as
323 reported earlier for ESAT-6 as well as other amyloidogenic proteins[42-44].
324 Subsequently, the phagosome numbers decrease over a few hours, suggesting the
325 disruption and cytosolic access of the ESAT-6 (Fig.3d). A striking fibrillar network
326 spanning the entire equatorial plane of the cell was visualized after 24 hours via live-
327 cell imaging through confocal as well as structured illumination microscopy suggesting
328 continued polymerization of the protein (Fig. 3e).
329

330 We next captured the changes in the phagosomal membrane shape and fibril
331 assembly at ultra-high resolution at the end of the fibrillation phase (i.e., ~24 hours)
332 using reconstituted large unilamellar vesicles. Negative-stain transmission electron
333 microscopy revealed polymeric fibrillar structures of ESAT-6 both in the presence and
334 absence of the phagosome membrane interface. ESAT-6 fibrils in the absence of

335 membrane seemed to have formed thicker bundles (Fig. 3g). In comparison to the
336 mother vesicle size ranging from 200-300 nm in diameter, most fields of view showed
337 significantly smaller vesicles in the range of ~ 40-70 nm tangled with ESAT-6 fibrils
338 (Fig. 3h-i and Extended Data Fig. 10). The area of contact of fibrils with the membrane
339 interfaces was found to be both radial and tangential (Fig. 3i). Many of the captured
340 vesicles also showed intact membrane bud necks in contact with the tip of the ESAT-
341 6 fibrils. Quantification of the fibril length revealed most fibrils to be around ~ 400-800
342 nm in length (Extended Data Fig. 9). This led us to question whether the ESAT-6
343 polymerization on the vesicular membrane interfaces is essential for fission. To
344 address this, we used dynamic light scattering to monitor the change of size of mother
345 vesicles in the presence of ESAT-6 over time. Monitoring the reaction containing 20
346 μM of ESAT-6 and LUVs (ranging ~ 1 μm in diameter) mimicking the phagosomal
347 membrane, revealed a significant peak shift from 1 μm to ~70-80nm at 24 hours (Fig.
348 3j). On the contrary, no significant change in the size was observed for membrane
349 only condition without ESAT-6 (Fig. 3f). Furthermore, both 1 μM & 5 μM of ESAT-6 did
350 not induce any shift in vesicle size suggesting no bud fission over the monitored period
351 of 30 hours (Fig. 3j). The ThT fluorescence kinetics of 1 μM & 5 μM of ESAT-6 on
352 phagosomal model membrane indeed showed a long nucleation phase without any
353 elongation phase confirming the absence of fibrillation (Extended Data Fig. 7). This
354 suggests that ESAT-6 fibrillation is essential for the observed fission of the buds and
355 the kinetics of the fission are dependent on the fibrillation rate that in turn depend on
356 the concentration of the protein.
357

358 ## The shape transitions of phagosomal membrane deformations are driven by
359 the polymerization forces of ESAT-6
360

361 We next examined the role of ESAT-6 fibrillation in inducing membrane deformation
362 and fission. The polymerization of proteins such as actin and β-microglobulin have
363 been reported to generate active forces in driving the transition of a flat membrane to
364 a bud [45, 46]. We used numerical simulations to capture the scaling between the
365 force generated by a growing network of ESAT-6 fibrils and membrane shape. The
366 polymerization of ESAT-6 results in the formation of fibrils with varying lengths (Fig.
367 3g-h). These fibrils interconnect to create a mesh or a network-like structure typical for
368 polymerizing proteins (Fig. 3h-i). We find that one end of the fibril remains attached to
369 the membrane either radially or tangentially (Fig. 3h-i), and hypothesize that the
370 polymerization at the other end exerts a ratcheting motion against the phagosomal
371 membrane. This ratcheting effect generates forces that play a role in shaping the
372 membrane[34-36]. To model the shape transition of the phagosomal membrane by
373 the ESAT-6 network, we employ Helfrich formalism[47] to account for the curvature-
374 mediated membrane energetics. We explicitly incorporate additional terms in the
375 Helfrich free energy to account for the forces exerted by the fibrils. Helfrich free energy
376 has been widely used to understand membrane surface deformation [46, 48-53].
377

In our model, the forces exerted by the fibrils include both vertical and radial components (Fig. 4a). The deformed membrane is assumed to exhibit axis-symmetry along the Z-direction (Fig. 3i). Furthermore, we model the double-layered structure as a monolayered surface, serving as a plausible mimic of the phagosomal membrane. The total energy of the membrane ($E$) is defined as

$$E = \int dA[2\kappa(C - C_0)^2] + \int dA\sigma + \int -d\boldsymbol{p}(F_R r + F_Z z) f(r, \theta, z(r)) \quad (2)$$

The first term in Eq. (2) represents the Helfrich bending energy functional, where $C$ stands for the mean curvature of the surface, $C_0$ for the intrinsic curvature, $\kappa$ for the bending rigidity, and $dA$ for infinitesimal area element of the membrane. The second term defines the energy due to surface tension where $\sigma$ represents the surface tension of the membrane. The last term accounts for the energy due to forces exerted by ESAT-6 fibrils, where $F_R$ and $F_Z$ represent the radial and vertical forces, respectively. In the last expression, $\boldsymbol{p} = (r, \theta, z(r))$, and $f\big(r, \theta, z(r)\big) = 1$ for the region of the membrane where the fibrillation force is acting; otherwise, $f\big(r, \theta, z(r)\big) = 0$ [46]. We minimize the free energy of the system by numerically solving Eq. (2) using Monte-Carlo simulated annealing [46, 53]. For details of the simulations, see Extended Data Text.

Because the binding of ESAT-6 in the phagosomal membrane is shallow, we expect that such binding would induce a localized intrinsic curvature at the binding sites. This leads to an observable deformation in the shape of the membrane (Extended Data Fig. 12). Additionally, we expect that as the surface density of ESAT-6 increases, the number of membrane-bound ESAT-6 fibrils will also rise significantly, resulting in a higher degree of deformation. We chose the vertical and radial forces in the order of pN to mimic biological forces as has been measured for actin and other polymerizing protein networks[34-36]. Systematically applying vertical forces ($F_Z$) induces changes in the membrane shape, leading to a noticeable increase in the size of the tubular bud (Fig. 4b-e). Furthermore, when radial forces ($F_R$) are introduced, a distinct neck forms along with a spherical bud (Fig. 3f-i). This highlights the significance of both vertical ($F_Z$) and radial ($F_R$) forces in reshaping the deformed membrane. Specifically, the vertical force regulates the size of the bud, while the radial force governs the shape, leading to the formation of a constricted neck. Our theoretical analysis suggests that the primary driver of membrane deformation is the forces generated due to ESAT-6 fibrillation. The outcome of this force-induced effect is the formation of a tubular bud, transitioning into a spherical bud, accompanied by the development of a distinct neck. Importantly, this specific shape configuration is crucial for facilitating the subsequent fission process, where the spherical bud detaches from the neck. EM images (Fig. 3h-i) show the co-occurrence of ESAT-6 fibrils meshed with the membrane and the corresponding deformation, thereby supporting our theory of fibrillation-driven membrane deformation. Additionally, the mere presence of free-standing tubular

420 necks without tension and strain did not undergo ESAT-6 mediated fission of the buds
421 (Fig. 4j), further confirming the fibrillation mediated fission.
422

## 423 ESAT-6 fibrils facilitate membrane fission by exerting forces that increase
## 424 areal strain and induce local lipid sorting

425
426 To validate the observations from the numerical simulations, we subjected the
427 membrane to stretching forces under equiosmolar conditions to rule out any potential
428 osmotic issues. Capturing the force exerted on the membrane by the polymerizing
429 ESAT-6 is technically limiting as fibrillation starts only after nucleation lag period of ~
430 20 hours *in vitro*. To circumvent this, a negative pressure of 50 Pascals that
431 corresponds to 0.5pN/$\mu m^2$ was applied to the phagosomal membrane GUV by
432 micropipette aspiration to mimic the exerted polymerization forces. Biological forces
433 generally operate in the order of pN as has been measured for actin and other fast
434 polymerizing protein networks[34-36]. A stable aspirated tongue length was obtained
435 in the case of the phagosomal membrane GUV that did not undergo any change in
436 the tongue length for the monitored duration of ~5 minutes (Fig. 5a & S5 - Movie).
437 Upon the injection of the unlabelled monomeric/lower oligomeric ESAT-6, the
438 aspirated tongue length gradually increased followed by an expanding lipid phase
439 separation area in the middle of the tongue (Fig. 5b & S6-Movie). The fluid lipids were
440 found to preferentially partition towards both the termini of the aspirated tongue as
441 evident from the enhanced Rhod-PE fluorescence. Rhod-PE is known to preferentially
442 partition into liquid disordered regions of the membrane resulting in enhanced
443 fluorescence intensity upon lipid segregation[54, 55]. As a result, a high curvature
444 tubular neck formed in the middle of the tongue before the fission and release of the
445 budded vesicle. Upon fission of the tip of the tongue, the remaining tongue relaxed
446 back to the GUV surface and retracted out of the micropipette. Using the Laplace law,
447 we then quantified the change in membrane tension induced by the ESAT-6, through
448 the relationship between surface tension and the pressure difference (Equation 3):
449

450 $$\tau = \Delta p(R_p . R_v)/2(R_v - R_p) \quad (3)$$

451
452 where $R_v$ is the radius of the vesicle and $R_p$ is the protrusion radius. Furthermore,
453 estimating the areal strain (i.e, area stretch modulus, $\Delta a/a_0$ ) exerted by the ESAT-6
454 interaction on a phagosomal membrane under high membrane tension using the
455 equation 4,
456

457 $$\Delta a/a_0 = R_p^2(1 + L_p/R_p)/2R_v^2 \quad (4)$$

458
459 revealed that there is a three-fold increase in the areal strain before the fission of the
460 bud (Fig. 5c & S6-Movie). Analysis of the relationship between change in tension and
461 areal strain revealed that while areal strain increased throughout the fission process,
462 the membrane tension increased up to the constriction point followed by relaxation

463 and attaining equilibrium after the vesiculation. The observed relative change in area
464 of the vesicle as a result ESAT-6 binding rules out any possibility of osmosis[56] (Fig.
465 5d). We next questioned whether the observed lipid phase separation under high
466 membrane tension is solely a consequence of stretching or could it also be induced
467 by the biochemical exchange of material between the bacteria and phagosomal
468 membrane under physiological conditions[57]. Direct contact of the Mycobacteria with
469 the phagosomal membrane is also considered important for phagosomal rupture in
470 addition to ESAT-6 [11]. To address this in real-time, we first reconstituted *in vitro* live
471 GFP-*Mycobacterium smegmatis* encapsulated inside a phagosomal membrane GUV.
472 The viability of the encapsulated bacteria was found to be 75 % by estimating the
473 colony-forming units by bacteria subjected to electro-formation conditions (Extended
474 Data Fig. 11). The encapsulated bacteria in direct-contact likely induced surface
475 adhesion of the GUV membrane lipids as evident from the merged fluorescence signal
476 at the area of contact (Fig. 5e). The direct contact also resulted in the local bending of
477 the membrane captured in z-stack (Fig. 5f). Additionally, a higher load of the
478 encapsulated bacteria inside the phagosome membrane GUV resulted in both shape
479 deformation as well as significant lipid phase separation wherein the Rhod-PE was
480 observed to preferentially enrich below the equatorial plane of the GUV (Fig. 5g-h,
481 time-lapse & z stack). Reconstituting phagosomal membrane mimic GUV containing
482 the lipids isolated from the mycobacterial cell envelope induced striking phase-
483 separated domains as evident from the preferential partitioning of Rhod-PE (Fig. 5i).
484 This suggests that material exchange as a result of direct-contact cannot be ruled out
485 as one of the potential factors inducing phase separation.
486
487 The observed membrane vesiculation *in vitro* as well as the fibrillation of ESAT-6
488 inside macrophage cells then led us to question the fate of the homeostatic state of
489 the cell. In line with the previous reports [8, 12, 58, 59], we observe that ESAT-6
490 induced a high rate of apoptosis as evident from the Annexin V-PI staining in a
491 concentration and time-dependent manner, which correlates with the observed in-vitro
492 fibrillation kinetics of the ESAT-6. (Fig. 6a). The high-resolution electron microscopy
493 captured significant morphological changes in the macrophage resulting in the
494 disintegration of the nucleus and cell membrane rupture which leads to the release of
495 cellular contents when treated with 20μM ESAT-6 and incubated for 24 hours
496 (Fig.6b&c). One of the peculiar observations was that most of the cells in different
497 fields of view appeared elongated in shape. This suggests that after the vesiculation
498 of the phagosomal membrane, ESAT-6 escapes into the cytosol and induces
499 apoptosis leading to cell death.
500
501 Together, we demonstrate that the initial binding of ESAT-6 induces tubular and bud-
502 like deformations by the reduction in the membrane tension. Both ESAT-6 binding and
503 direct contact with Mycobacterium induced lipid segregation in the membrane which
504 might be important for the rupture of the phagosome. The forces exerted by the ESAT-
505 6 polymerization increase the membrane tension accompanied by the rise in areal

506 strain that drives the vesiculation of the phagosomal membrane, subsequently,
507 inducing apoptosis and host cell death.
508

509 ## Discussion
510
511 In this study, we investigated the mechanism by which the *Mtb* secretory protein,
512 ESAT-6, deforms the phagosome membrane for the escape and survival of the
513 bacteria. We demonstrate that the binding of ESAT-6 on the phagosome membrane
514 mimic is concomitant with the reduction in the overall membrane tension that facilitates
515 the vesiculation of the phagosome membrane in a fibril-dependent manner. While the
516 ESAT-6 is sufficient to induce membrane budding in its lower oligomeric form, the
517 vesiculation of the membrane buds predominantly occurs only upon the
518 polymerization of ESAT-6 into fibrils. The phagosome disruption is one of the key
519 aspects in the arrest of the phagosome maturation and the egress of Mycobacteria [2,
520 60]. It is reported that *Mtb* ruptures the phagosome membrane and escapes after 48
521 hours through an ESAT-6-mediated phagosome lysis [6, 7]. ESAT-6, the major
522 secretory protein of ESX-A is membrane-lytic that mediates phagosome rupture,
523 however, the molecular mechanism remains elusive [2, 11, 13, 60]. Though the
524 oligomeric state of the ESAT-6 complex is yet to be determined, it is reported to insert
525 as a membrane-spanning protein that provides the foundation for pore formation
526 based on haemolysis assay [5, 9, 10]. An important reason behind the observed
527 membrane-spanning pore-forming conformation could be the usage of oversimplified
528 lipid composition, that is, DOPC. The packing density arising due to the cylindrical
529 geometry of the DOPC may facilitate the deep insertion of the ESAT-6 [61] but might
530 not be the case for a complex multi-component biological membrane [42]. On the
531 contrary, we show that ESAT-6 inserts only until C5 of the acyl chain, on biologically
532 relevant phagosomal membrane mimic comprising lipid composition of complex
533 geometry. Pore formation may occur transiently as an intermediate step, owing to
534 weak binding to the membrane as confirmed by high $K_d$ as well as diffusion (Fig.1b, f
535 ). Unlike the ESX-E/F secretory proteins and other pore forming proteins, there is no
536 concrete experimental evidence for pore formation by the oligomeric assembly of
537 ESAT-6 [62-65]. Indeed, the changes in the conductance pattern induced by ESAT-6
538 measured on artificial lipid bilayers suggest a non-uniform fluctuation and was
539 speculated due to the amyloidogenic properties of ESAT-6 as also seen in some
540 bacterial toxins [26, 39]. ESAT-6 binding to membrane at low and high surface
541 densities induced shape transition from slightly curved to tubular structures (Fig 1c-d)
542 and membrane buds. The binding of the protein makes the phagosome membrane
543 more deformable enabling the generation of curved protrusions as evident from the
544 ESAT-6-induced reduction in the compressibility modulus of the phagosome and
545 membrane tension (Fig. 2e, Fig. 2a-c). However, the buds do not detach from the GUV
546 surface until 24 hours (Fig 2g-h). Further, an increase in polarity was observed over
547 24 hours resulting from the larger proximity of deformed interfacial regions to water
548 moieties quantified by the lifetime changes of Tryptophan residues of ESAT-6 (Fig. 2j-
549 k). The observed tubulations and buds can be attributed to the changes in local
550 membrane curvature and lateral pressure introduced as a result of high surface
551 density and shallow insertion of ESAT-6 pushing away the lipid-head groups in the
552 interacting membrane leaflet[66-69]. Indeed the magnitude of the protein-induced

553 membrane bending and curvature generation is known to non-monotonously depend
554 on the insertion depth of the protein for biologically relevant conditions [68, 70].
555 Shallow embedding of amphipathic helices has been shown to induce formation of
556 tubes of varying sizes. For example, while epsin and synaptotagmin forms narrow ~
557 20nm diameter tubes [71, 72], N-BAR containing endophilin and amphiphysin
558 generate tubes ranging ~ 35-50nm in diameter that subsequently form vesicles of the
559 same size [73]. Recently, tubulation and budding was reported in the phagolysosomes
560 containing *E. coli* important for lysosomal reformation during phagosome resolution
561 [74].
562
563 We then wondered why the detachment of the membrane buds takes around 24 hours
564 (Fig 2i). ESAT-6 is known to form amyloid-like structures in the inclusion bodies of *E.*
565 *coli* making the kinetics of transition much faster [39]. However, very recently ESAT-6
566 has been shown to undergo rapid self-association though lacking any evidence of
567 fibrillation [43]. ESAT-6 indeed gets phagocytosed upon treatment with THP-1 derived
568 macrophage, and subsequently fibrillates and deforms the phagosomal membrane.
569 Further, upon gaining access to the cytosol it continues to polymerize into a strong
570 network of fibrils spreading throughout the cell (Fig 3e). We provide the first evidence
571 supporting fibrillation of ESAT-6 inside the macrophage phagosome. The decrease in
572 the number of phagosome as a result of elevated concentration of ESAT-6 inside the
573 phagosome suggests that the kinetics of the disruption may vary *in vivo* and *in vitro,*
574 depending on the local concentration of the protein. Interestingly, we observe that
575 ESAT-6 fibrillates in the presence of phagosome membrane interface that slows down
576 the fibrillation kinetics and forms a mesh-like network at the equilibrium phase (Fig 3a-
577 c, 3h-i). It is important to note that until the equilibrium phase is reached, ESAT-6
578 would exist as a mixture of monomers, oligomers, and fibrils, all of which can bind to
579 the membrane with different affinities and deform the membrane [42, 44]. Both the
580 high surface density of the protein and the growing network of polymerizing protein
581 are known to exert forces on the membranes resulting in local modulation of curvature
582 and tension [45, 75-78]. However, lowering the concentration of ESAT-6 to slow down
583 or abort the polymerisation showed no vesiculation, indicating that polymerisation is
584 essential for vesiculation. Keeping the membrane under elevated tension through
585 aspiration to mimic the fibril-mediated force generation, binding of oligomeric ESAT-6
586 triggers membrane fission accompanied by an increase in the membrane tension and
587 areal strain (Fig. 5b). This might be facilitated by both direct bacterial contact and
588 curvature-driven lipid sorting aided by ESAT-6, as the phagosomal lipid composition
589 is close to the demixing point also observed for endocytic proteins [79, 80]. We
590 propose that the fibrillation of ESAT-6 inside the phagosome might induce vesiculation
591 of the membrane resulting in decrease in the surface area/volume ratio (Figure 7). And
592 this persistent vesiculation eventually induces apoptosis, thus aiding the
593 mycobacterial escape and spread to other neighbouring cells promoting infection. The
594 role of apoptosis during *M.tb* infection is debated [81-85], however, by modulating the
595 concentration of the secreted ESAT-6 inside the phagosome, *M.tb* may regulate its
596 own residency time. The proposed mechanism explains the variation in the

phagosomal escape time observed for Mycobacteria and could be crucial for the pathogenesis.

607 ## Methods
608
609 **Materials**
610 1,2-dioleoyl-*sn*-glycero-3-phosphocholine (DOPC), 1,2-dioleoyl-*sn*-glycero-3-
611 phosphoethanolamine (DOPE), BSM, di-stearoyl phosphatidyl ethanolamine-PEG
612 (2000)-biotin and cholesterol were purchased from Avanti Polar Lipids. Fluorescent
613 conjugated lipid lissamine rhodamine B sulfonyl (Liss Rhod PE) was also purchased
614 from Avanti Polar Lipids. Avidin coated on the chamber slides was purchased from
615 Sigma-Aldrich. ESAT-6 was labeled using the FITC labeling kit purchased from
616 Sigma-Aldrich and labeled using the standard protocol. Proteins were aliquoted in
617 PBS (1X) and stored at -80°C.
618
619 **Preparation of GUV**
620 The phagosomal membrane mimic GUVs were composed of 40% DOPC, 5.5%
621 DOPE, 22%BSM, 32.5% cholesterol, 0.03% PEG-Biotin, and 0.1% Rhod PE. To
622 achieve a satisfactory yield of GUVs, the electroformation was performed as described
623 in [23]. In summary, a uniform coat of 15μL of lipid mix at 5 mg $ml^{-1}$ was first dried on
624 conductive indium-tin oxide-coated glass (Nanion technologies, GmbH) under vacuum
625 for at least 1 h. The lipid film was then rehydrated in a PBS (pH 5.5) at 300 ±5 mOsm
626 and GUVs were allowed to grow for 3 h under a sine voltage (2V, 10 Hz) at 60°C. For
627 encapsulation of the live Mycobacteria inside GUVs, the lipid film was rehydrated using
628 7H9 media with precultured Mycobacteria of OD 1-1.2.
629
630 **Overexpression and purification of ESAT-6**
631 E. coli BL21 (DE3, plysS) strain was utilized for the expression and purification of
632 ESAT-6. The strain was transformed with the plasmid pET22b, which included the M.
633 tb gene Rv3875 (protein ESAT-6). The transformed bacteria were grown in LB medium
634 at 37 °C, and protein expression was done at OD600 nm~0.6, induced by adding 1
635 mM of isopropyl -D galactopyranoside (IPTG) overnight at 18 °C. Following, bacterial
636 cells were pelleted, and sonicated, and the (His)6-tagged protein was purified using
637 affinity chromatography with Nickel nitrilotriacetic acid (Ni-NTA) according to the
638 manufacturer's recommendations (GE Healthcare, UK). SDS-PAGE analysis
639 validated the purification of rESAT-6. The purified fractions were dialyzed,
640 concentrated, and kept in aliquots at -80 °C until further use.
641
642 **Fluorescence quenching assay**
643 The interaction of ESAT-6 with the phagosomal membrane was observed through the
644 intrinsic fluorescence of Tryptophan residue in ESAT-6. To measure the fluorescence
645 intensity 5μM of ESAT-6 was equilibrated for 5 minutes with increasing lipid
646 concentrations. The excitation wavelength was fixed at 290 nm and the emission
647 spectra were collected between 300-400 nm at a constant temperature of 25 °C. All
648 the fluorescence measurements were performed with an FLS 1000 (Edinburg
649 Instruments, UK) spectrophotometer using a quartz cuvette with a 1cm path length.

650

**Light Microscopy**

8 Well chamber slide from Ibidi was coated with 10µl of 1mg/ml streptavidin, and 200µL of biotinylated GUVs was added and incubated for 15 mins for the GUVs to be immobilized. The final concentration of 5µM of FITC-ESAT-6 was added into the chamber. Imaging was performed on Leica TCS SP8 LCSM using an appropriate laser for Rhodamine-PE (561nm) and Alexa-488 (488nm). Identical laser power and gain settings were used during all experiments.

For the Fluorescence recovery after photobleaching (FRAP) measurements on the GUVs, the GUVs were doped with 0.1% of rhodamine PE and were incubated with 5 µM of ESAT-6. Initially images were captured at reduced laser intensity. Photobleaching was performed at full laser intensity for 30 seconds, resulting in the bleaching within the selected ROI of radius of 5µm. Subsequently, the laser intensity was reverted to the attenuated level and the recovery curve was recorded.The photobleaching was performed at the equatorial plane of the GUV being visualized. The FRAP curves for each condition were repeated three times and then normalized. The diffusion coefficient was calculated using the Soumpasis equation for 2D diffusion

$$D_R = 0.224 \frac{R^2}{\zeta_{1/2}} \tag{5}$$

where 0.244 is the numerically determined value, r (5 µm) stands for the radius of the laser beam focused on the region of interest, and τ1/2 is the time required for half the recovery. The time for half the recovery was determined by plotting the normalized recovery curve.

For the in-vivo experiments, the human monocyte cell line (THP-1) was incubated overnight with PMA along with the RPMI to differentiate into the macrophages. Cells were labeled with NIT-OH, a red fluorescent labelling dye. Followed by the treatment with the 20µM FITC-ESAT-6 on the cells and super-resolution images were taken after 24 hours of incubation with the 488nm laser on Zeiss Elyra7.

**Fluorescence Lifetime Imaging**

Fluorescence lifetime imaging microscopy was performed on an MT200 (Pico Quant, Berlin, Germany) time-resolved fluorescence confocal microscope with a Time-Correlated Single Photon Counting (TCSPC) unit. The laser power was adjusted between 10 to 100nW for 488nm laser light measured after the dichroic mirror. The Well glass bottom slide was directly placed on immersion water of 60x objective. A dichroic mirror of 488nm was used as the main beam splitter. Out-of-focus emission light was blocked by a 50 µm pinhole and the in-focus emission light was then split by a 50/50 beam splitter into two detection paths. Single Photon Avalanche Diodes (SPADs) served as detectors. Both data acquisition and analysis were performed on the commercially available software Sympho Time 64 (Pico Quant GmbH, Berlin, Germany).

**Time resolved fluorescence measurements**

Time-resolved fluorescence intensity decays were obtained by using IBH 5000F Nano LED equipment (Horiba, Edison, NJ) in the time-correlated single photon counting (TCSPC) mode. The excitation source of a pulsed light-emitting diode (LED) was used. At 290nm optical pulses were generated by this LED with a pulse duration of 1.2 ns and emission was measured at 335nm with 1 MHz repetition rate. The Instrument Response Function (IRF) was quantified at the respective excitation wavelength using Ludox (colloidal silica) as a scatterer. 10,000 photon counts were collected in the peak channel to optimize the signal-to-noise ratio. The lifetime of tryptophan residue of ESAT-6 was performed using emission slits with a bandpass of 8 nm. Data were examined using DAS 6.2 software (Horiba, Edison, NJ). Fluorescence intensity decay curves were developed with the IRF and measured using:

$$F(t) = \sum_{i}^{n} \alpha_i \exp\left(-\frac{t}{\tau_i}\right)$$

All the plots were quantified with a random deviation of about zero with a maximum $\chi^2$ value of 1.2 or less. Intensity averaged mean lifetimes $\tau_{avg}$ for fluorescence exponential decays were obtained from the decay times and pre-exponential factors using the following equation

$$\tau_{avg} = \frac{\sum \alpha_i {\tau_i}^2}{\sum \alpha_i \tau_i}$$

where $\alpha_I$ shows the fraction of $\tau_i$ lifetime.

**Thioflavin T Assay to determine kinetics of protein aggregation**

The aggregation kinetics of ESAT-6 was monitored by ThT fluorescence as a function of time. The final monomeric ESAT-6 concentration was 20μM and 50μM was diluted in PBS solution (Ph-5.5) which comprises 200μM of LUV and 50μM of ThT dye. All the samples were incubated at 37°C in NUNC 96 well plate throughout the experiment. The plate was loaded into the 96-well Clariostar microplate reader equipped with 448/482-nm excitation/emission filters and the ThT fluorescence intensity was monitored every 15 minutes of 500 cycles.

**Lipid Monolayer experiments**

The monolayer experiments were performed in KSV NIMA Langmuir balance. The instrument consisted of two barriers used during the compression isotherms assays and as a surface pressure sensor a Wilhelmy microbalance with filter paper plate was used. Monolayers of DOPC: DOPE:SM: CHOL were formed by spreading the lipid/chloroform solution (1mg/ml) in a dropwise manner and kept for 15 mins to equilibrate the monolayers and for the evaporation of the chloroform. PBS (Ph-5.5)

was used as the subphase with the maintained temperature of 25°C for all the Langmuir experiments. The final working concentration of 5μM ESAT-6 was injected into the monolayer for isotherm assays. Isotherms were recorded with uniform compression of the monolayer at a constant speed of 1 mm/min. Isotherms were recorded until collapse pressure (πc) was reached. For constant area assays (Time v/s surface Pressure), the monolayer is initially compressed to 30mN/m and allowed to equilibrate for 15 minutes. ESAT-6 was then injected into the subphase and the change in the surface pressure over time was recorded. For all the Langmuir experiments, the trough was cleaned thoroughly with ethanol and filtered double-deionized water until zero surface pressure was reached. Each experiment was performed thrice.

**Negative Staining & Transmission Electron Microscopy**

10μl of the fibrillated ESAT-6 with LUVs was incubated in the carbon-coated grid for 20 minutes and wicked off with the help of qualitative filter paper from Himedia. Then 10μl of 2.5% glutaraldehyde was added to the grid for fixation of the sample. The carbon-coated grid was then rinsed using deionized water and 10μl of uranyl acetate was added. After the incubation of 3 minutes and rinsing the grid with deionized water. The grid was then vacuum-dried overnight. The imaging was performed on a JEOL (JEM 2100F) transmission electron microscope. For the cell-based experiments, ThP1-derived macrophages were treated with Esat-6 and incubated for 24 hours. Cells were washed with 0.1M phosphate buffer to get rid of cell culture media and processed for EM as described previously [86]. Briefly, cells were fixed with primary fixative (2.5% glutaraldehyde, 1.25% paraformaldehyde, and 0.1 M phosphate buffer, pH 7.0) for 15 min at RT. Cells were harvested and again resuspended in 1 ml fresh fixative media and incubated on ice for 1 hour. Cells were washed with 0.1M phosphate buffer followed by post-fixation with 1% osmium tetroxide ($OsO_4$) in 0.1 M phosphate buffer for 1 hour at RT followed by washing with distilled water twice. Next, cells were incubated with 1% uranyl acetate for 1 hour at RT. Subsequently, samples were dehydrated by incubating in increasing concentrations of ethanol (30%, 50%, 70%, 80%, 90%, 95%, and 100%) for 10 minutes each, with two more incubations in 100% ethanol from a freshly opened bottle. The samples were subsequently embedded stepwise using Spurr's low-viscosity resin (EMS). Samples were infiltrated for 2 h each with a 3:1, 1:1, 1:3 ethanol / embedding media mixture. Cells were incubated overnight with 100% fresh resin. The next day, cells were again resuspended in fresh 100% resin for 2–3 h, transferred into BEEM capsules (EMS), and polymerized at 70°C for 4 days. Semi- and ultrathin sections were produced with a diamond knife (Diatome) on an ultramicrotome (Ultracut UCT; Leica Microsystems), collected on 200 mesh copper grids (EMS), poststained with uranyl acetate and lead citrate, and visualized with a Talos S200 transmission electron microscope (TEM; Thermo Fisher Scientific), operating at 200 kV. Pictures were recorded on a below-mounted 4k × 4k BM-Ceta (CMOS) camera.

**Micropipette Aspiration**

All the measurements were performed on an Olympus IX83 epifluorescence microscope equipped with the Hoffman modulation optics and observed on the 100X objective lens. For positioning the pipette three-axis hydraulic micro-manipulators are used. Micro-pipettes are pulled (Sutter Instruments CO P-87, Narishige Micro forge MF-900) from 10μm diameter capillaries. 100 μl of GUVs were added to the open homemade coverslip. The desired suction pressure for aspirating a GUV is provided, causing the vesicle to be aspirated through the micropipette tip and develop an inner protrusion. Over the period video was recorded to determine the vesicle geometry on the addition of the ESAT-6.

**Subcellular fractionation and lipid extraction of Mycobacterial cell envelope**

The *M. smegmatis* were grown in 7H9 broth under continuous shaking for 3 days at 37° C. For subcellular fractionation, the culture was centrifuged at 4400g to obtain the bacterial pellet and carried out following the procedure outlined in [87]Briefly, the bacterial pellet was subjected to mechanical disruption twice using a French press followed by the bead beater by using microbeads (Himedia) to break the cells. Furthermore, the cells were lysed 2-3 times with beads and then centrifuged at low spin to remove unbroken cells. The supernatant was centrifuged 3- 5 times at 27000g for 40 minutes to pellet the cell wall. The supernatant obtained previously was then ultracentrifuged at 100,000×g for 1 hour to obtain the cell membrane in the pellet fraction. Finally, the cell wall and cell membrane fractions were resuspended in PBS at a 1:1 ratio and stored in aliquots at -80°C.

Lipid extraction from the mycobacterial cell envelope was done by using the Folch method as described in[88]. The cell envelope was dried with nitrogen gas and kept in a vacuum overnight. The dried cell envelope was mixed with chloroform and then sonicated for 30 minutes at a constant pulse. The solution was again dried and chloroform and ice-cold methanol were subsequently added to the 2:1(V/V) ratio to the sample. After incubation in ice for 20 minutes same amount of distilled water was added as methanol and kept in ice for 10 minutes followed by centrifugation at 1500rpm for 5 minutes to separate the upper polar part containing salt and proteins and the lower organic phase containing lipids. The lower organic phase was dried using nitrogen gas and stored at -80°C.

**Image & Statistical Analysis**

The ImageJ software was used to analyze and process images. The fluorescent intensity plots along the equatorial plane of GUVs were quantified using the average fluorescence intensity of the membrane ($F_{vesicle}$) by subtracting the background intensity ($F_{background}$). A uniform detection setting was applied for all sets of experiments. Vesicle sizes were quantified manually using ImageJ. Statistical significance was calculated through one-way ANOVA in sigmaplot where p-values less than 0.05 were considered statistically significant throughout all the experiments.

824
825

# Figures & Figure Legends

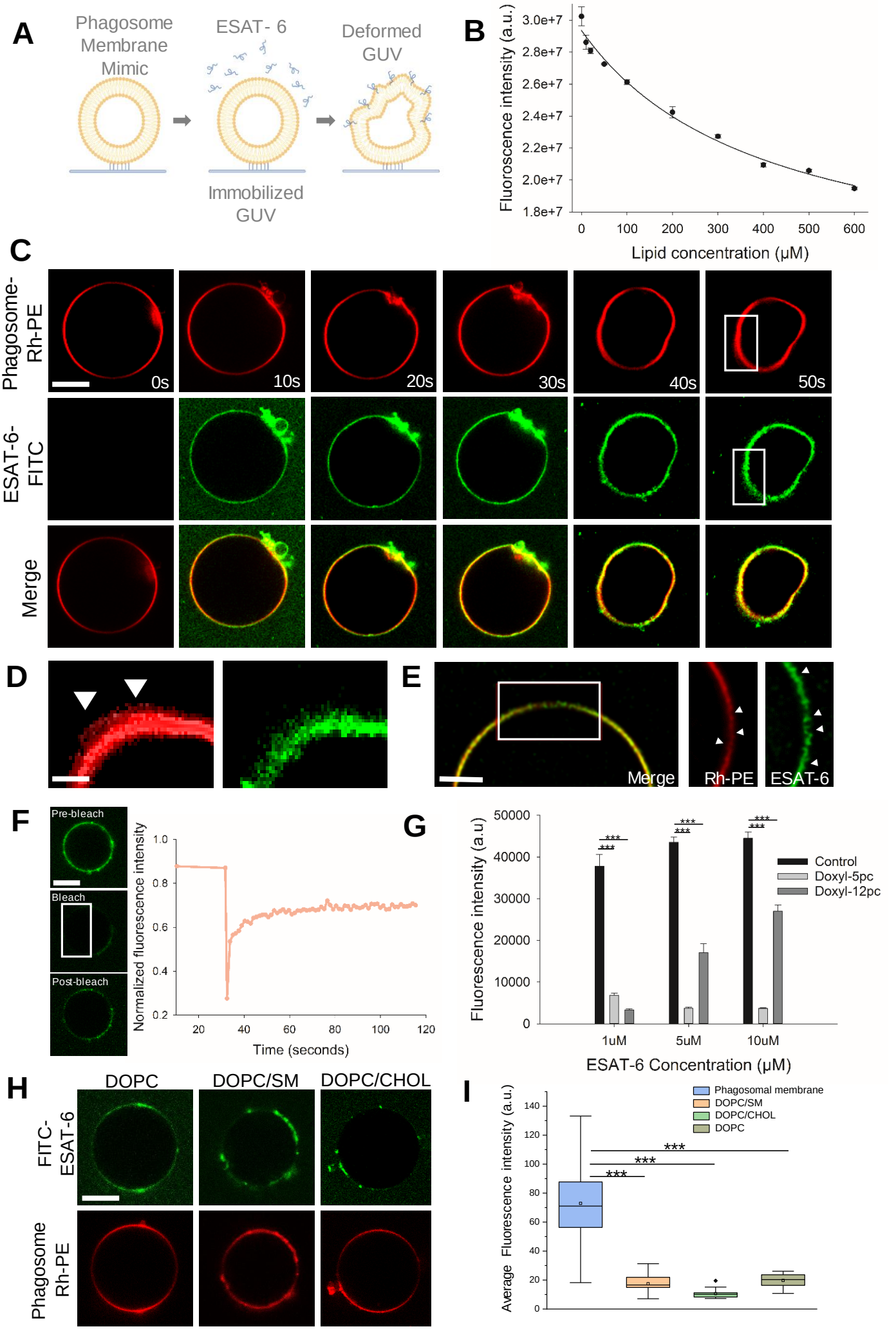
A
Phagosome Membrane Mimic
ESAT- 6
Deformed GUV
Immobilized GUV
B
Fluorescence intensity (a.u.)
3.0e+7
2.8e+7
2.6e+7
2.4e+7
2.2e+7
2.0e+7
1.8e+7
0
100
200
300
400
500
600
Lipid concentration (μM)
C
Phagosome-Rh-PE
ESAT-6-FITC
Merge
0s
10s
20s
30s
40s
50s
D
E
Merge
Rh-PE
ESAT-6
F
Pre-bleach
Bleach
Post-bleach
Normalized fluorescence intensity
1.0
0.8
0.6
0.4
0.2
20
40
60
80
100
120
Time (seconds)
G
Fluorescence intensity (a.u)
50000
40000
30000
20000
10000
0
***
Control
Doxyl-5pc
Doxyl-12pc
1uM
5uM
10uM
ESAT-6 Concentration (μM)
H
DOPC
DOPC/SM
DOPC/CHOL
FITC-ESAT-6
Phagosome Rh-PE
I
Average Fluorescence intensity (a.u.)
140
120
100
80
60
40
20
0
Phagosomal membrane
DOPC/SM
DOPC/CHOL
DOPC
***

826 **Figure 1. Shallow insertion of ESAT-6 induces changes in phagosomal**
827 **membrane curvature. a,** Schematic representation of experimental design depicting
828 deformation of the immobilized GUV mimicking the phagosomal membrane by ESAT-
829 6**. b,** Fluorescence intensity plot of tryptophan residue of ESAT-6 as a function of lipid
830 concentration (LUVs), fitted using hyperbolic decay from sigma plot. Experiments were
831 carried out in PBS pH 5.5 at 25 °C. ESAT-6 concentration was kept constant at 5μM.
832 Data points shown are means ± S.D. of three independent measurements**. c,** Time-
833 lapse confocal imaging of GUVs labeled with 0.1% Rh-PE (red) and immobilized using
834 0.03% PEG-Biotin incubated with 5μM FITC-ESAT-6 (green). Scale bar, 5μm. Images
835 are the representative of five independent experiments (n=73 GUVs). **d,** zoomed
836 images extracted from **c** represent the curvature change on the membrane. **e,**
837 Structured illumination microscopy (SIM) images of GUVs with the same condition as
838 in **c** followed by zoomed images of the change in membrane curvature. Scale bar,
839 5μm (n= 15 GUVs). **f,** Mean fluorescence recovery curve after photobleaching
840 experiments of 5μM FITC-ESAT-6 on the membrane. Data points using mean values
841 from three independent experiments. **g,** Fluorescence intensity plot of tryptophan
842 residue of ESAT-6 interaction with LUVs (100nm sizes) containing 10mol% of 5-doxyl-
843 PC and 12-doxyl-PC. Data points shown are means ± S.D. of nine measurements
844 from three independent experiments. **h,** confocal imaging of GUVs of DOPC,
845 DOPC/cholesterol, and DOPC/SM labeled with 0.1% Rh-PE (red) and immobilized
846 using 0.03% PEG-Biotin incubated with 5μM FITC-ESAT-6 (green). Scale bar, 5μm.
847 Images are the representative of five independent experiments (n=25 GUVs). **i,** Mean
848 fluorescence intensity plot of ESAT-6 binding for each membrane condition
849 (***$p<0.001$ in one-way ANOVA).
850

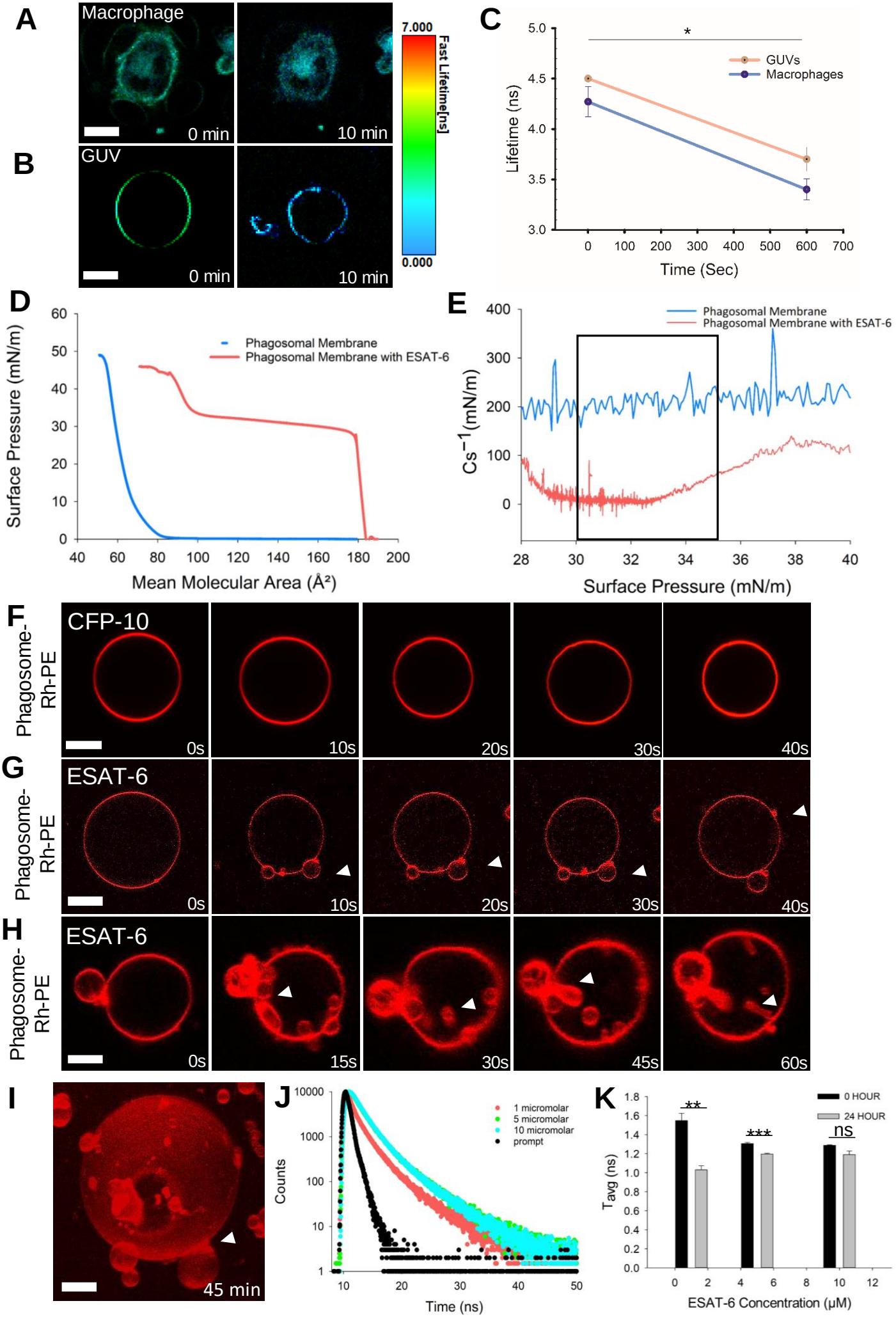
A
Macrophage
0 min
10 min
B
GUV
0 min
10 min
7.000
Fast Lifetime[ns]
0.000
C
GUVs
Macrophages
Lifetime (ns)
Time (Sec)
D
Phagosomal Membrane
Phagosomal Membrane with ESAT-6
Surface Pressure (mN/m)
Mean Molecular Area (Å²)
E
Phagosomal Membrane
Phagosomal Membrane with ESAT-6
Cs⁻¹(mN/m)
Surface Pressure (mN/m)
F
CFP-10
Phagosome-Rh-PE
0s
10s
20s
30s
40s
G
ESAT-6
Phagosome-Rh-PE
0s
10s
20s
30s
40s
H
ESAT-6
Phagosome-Rh-PE
0s
15s
30s
45s
60s
I
45 min
J
1 micromolar
5 micromolar
10 micromolar
prompt
Counts
Time (ns)
K
0 HOUR
24 HOUR
Tavg (ns)
ESAT-6 Concentration (μM)

851 **Figure 2. ESAT-6 binding reduces phagosomal membrane tension and**
852 **compressibility modulus and induces budding at higher surface density.** Images
853 from fluorescence lifetime imaging microscopy (FLIM) of FliptR-labelled **a,** live
854 macrophages, and **b,** phagosomal membrane mimic GUV before and after 10 min of
855 5μM ESAT-6 treatment. **c,** FliptR lifetime measurements of live macrophages and
856 GUV from three independent experiments as shown in **a,b**. the data points shown are
857 means ± S.D (*p<0.05 in one-way ANOVA).**d,** surface pressure (π)– mean molecular
858 area (A) isotherm of the phagosomal membrane in the absence(blue) and presence
859 of ESAT-6 (red). **e,** compressibility moduli ($Cs^{-1}$) at a surface pressure of 30-35mN/m
860 (at the bilayer equivalence pressure marked in the rectangular box) is shown in the
861 graph with the same labeling order and color scheme for the membrane conditions as
862 stated in **d.** All the monolayer experiments were performed on PBS subphase pH 5.5
863 at 25°C. Each isotherm corresponds to the mean of three independent experiments.
864 Time-lapse confocal imaging of immobilized GUVs (same composition and labeling as
865 in **fig.1c**) in the presence of higher concentration(20μM) **f,** CFP-10 and **g,h,** ESAT-6.
866 Scale bar, 5μm (n=14 GUVs for CFP-10 and n=18 GUVs for ESAT-6). **i,** 3D projection
867 of budded vesicles on the membrane extracted from the **g. j,** Time-resolved
868 fluorescence intensity decay plots of 1 (red), 5 (green), and 10 μM (blue) of ESAT-6,
869 respectively, in the presence of phagosomal membrane mimic LUVs and measured
870 after 24 hours. The fluorescence decay plot of the instrument response function (IRF)
871 is shown in black. All the measurements were carried out in PBS (pH 5.5) at 25°C.
872 These are the representative curves from three independent experiments. **k,** the mean
873 fluorescence lifetime plot extracted from **j** and time-resolved fluorescence intensity
874 decay plots of 1 (red), 5 (green), and 10 μM (blue) of ESAT-6, respectively, in the
875 presence of phagosomal membrane mimic LUVs and measured after 30 minutes
876 (reference, 0 hr)**,** and the data points shown are means ± S.D. of three independent
877 measurements (**p<0.01, ***p<0.001 in one-way ANOVA).
878

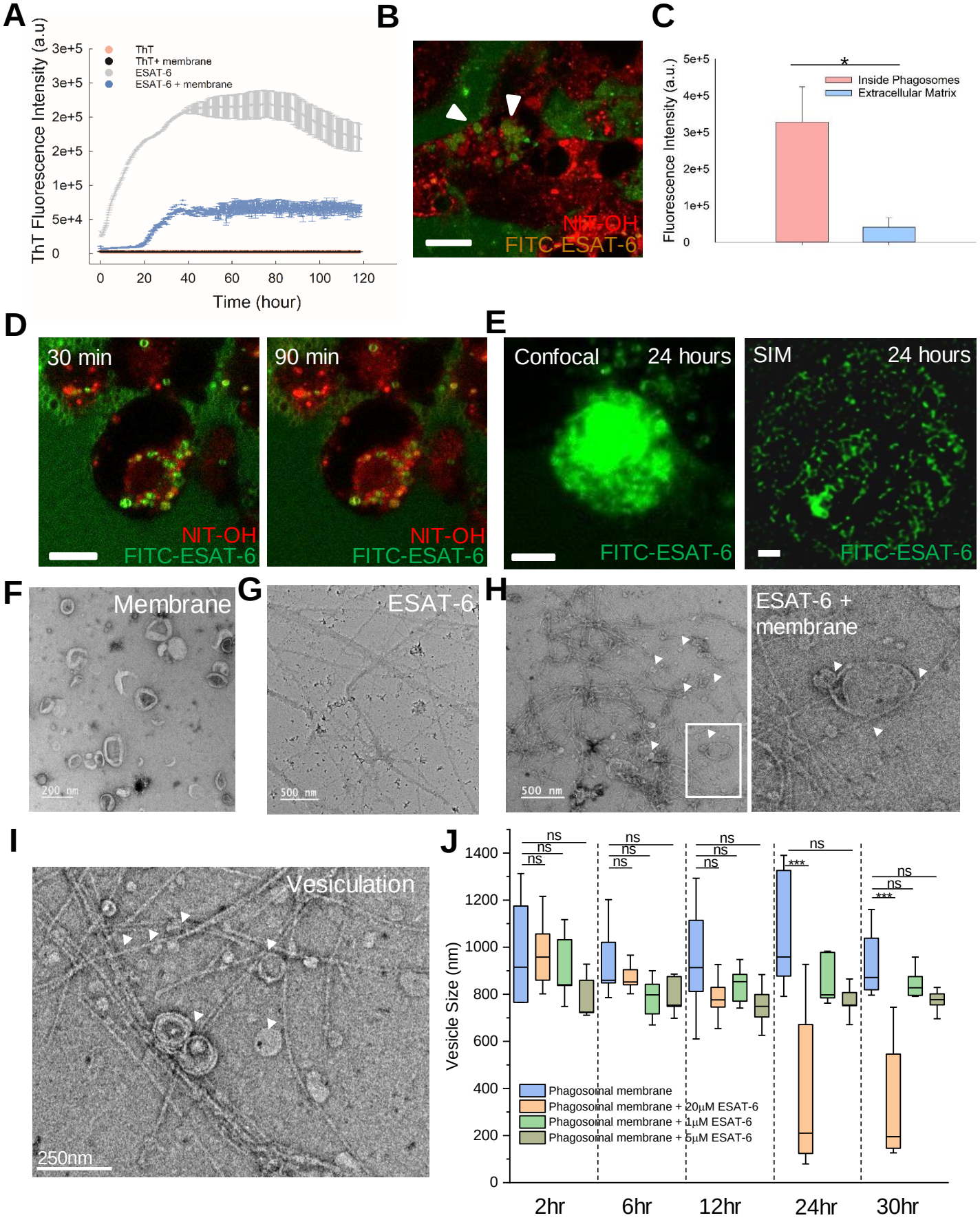
A
ThT Fluorescence Intensity (a.u)
3e+5
3e+5
2e+5
2e+5
1e+5
5e+4
0
ThT
ThT+ membrane
ESAT-6
ESAT-6 + membrane
0
20
40
60
80
100
120
Time (hour)
B
NIT-OH
FITC-ESAT-6
C
Fluorescence Intensity (a.u.)
5e+5
4e+5
3e+5
2e+5
1e+5
0
*
Inside Phagosomes
Extracellular Matrix
D
30 min
NIT-OH
FITC-ESAT-6
90 min
NIT-OH
FITC-ESAT-6
E
Confocal
24 hours
FITC-ESAT-6
SIM
24 hours
FITC-ESAT-6
F
Membrane
200 nm
G
ESAT-6
500 nm
H
500 nm
ESAT-6 +
membrane
I
Vesiculation
250nm
J
Vesicle Size (nm)
1400
1200
1000
800
600
400
200
0
ns
***
Phagosomal membrane
Phagosomal membrane + 20μM ESAT-6
Phagosomal membrane + 1μM ESAT-6
Phagosomal membrane + 5μM ESAT-6
2hr
6hr
12hr
24hr
30hr

**Figure 3. ESAT-6 polymerization facilitates phagosomal membrane vesiculation.** **a,** ThT fluorescence assay of only 20μM ESAT-6 (gray) and in the presence of phagosomal membrane mimic LUVs (blue) as a function of time. Data points are shown as the means ± S.D. of three independent measurements. All the experiments are carried out on PBS pH 5.5 at 37°C**. b,** Thp-1 derived macrophages stained with NIT-OH (red) treated with FITC-ESAT-6 (green) showing the biogenesis of ESAT-6 encapsulated phagosomes (highlighted through arrows). Scale bar, 15μm. **c,** Quantification of FITC-ESAT-6 fluorescence intensity through ImageJ of ESAT-6 encapsulated phagosomes (n=150) and extracellular matrix. **d,** Time-lapse imaging of live cell stained by NIT-OH (red) showing ESAT-6 encapsulated phagosomes (green). Scale bar, 15μm. **e,** Confocal images and structured illumination microscope (SIM) images of Thp-1 derived macrophages with 20μM FITC-ESAT-6 incubated for 24 hours. Mesh-like network formed inside cells. Representative images from total number of 87 cells observed in different fields of views. Transmission electron micrographs capturing the shape change of membrane during ESAT-6 fibrillation as shown in **f,** only LUVs (Scale bar, 200nm), **g,** ESAT-6 fibrils (white arrows), and **h,** the budding and vesiculation (white arrows) marked inset images on bottom, **i,** Mesh like network of ESAT-6 fibrils around the mother and daughter vesicles. Scale bar, 500nm. **h,** Vesicle size quantified through dynamic light scattering experiment of only LUVs (blue) and LUVs in the presence of 20 μM (peach),1 μM (green), and 5 μM (dark green) of ESAT-6 monitored for 30 hours. The data points shown are means ± S.D. of three independent measurements (**$p<0.01$, ***$p<0.001$ in one-way ANOVA).

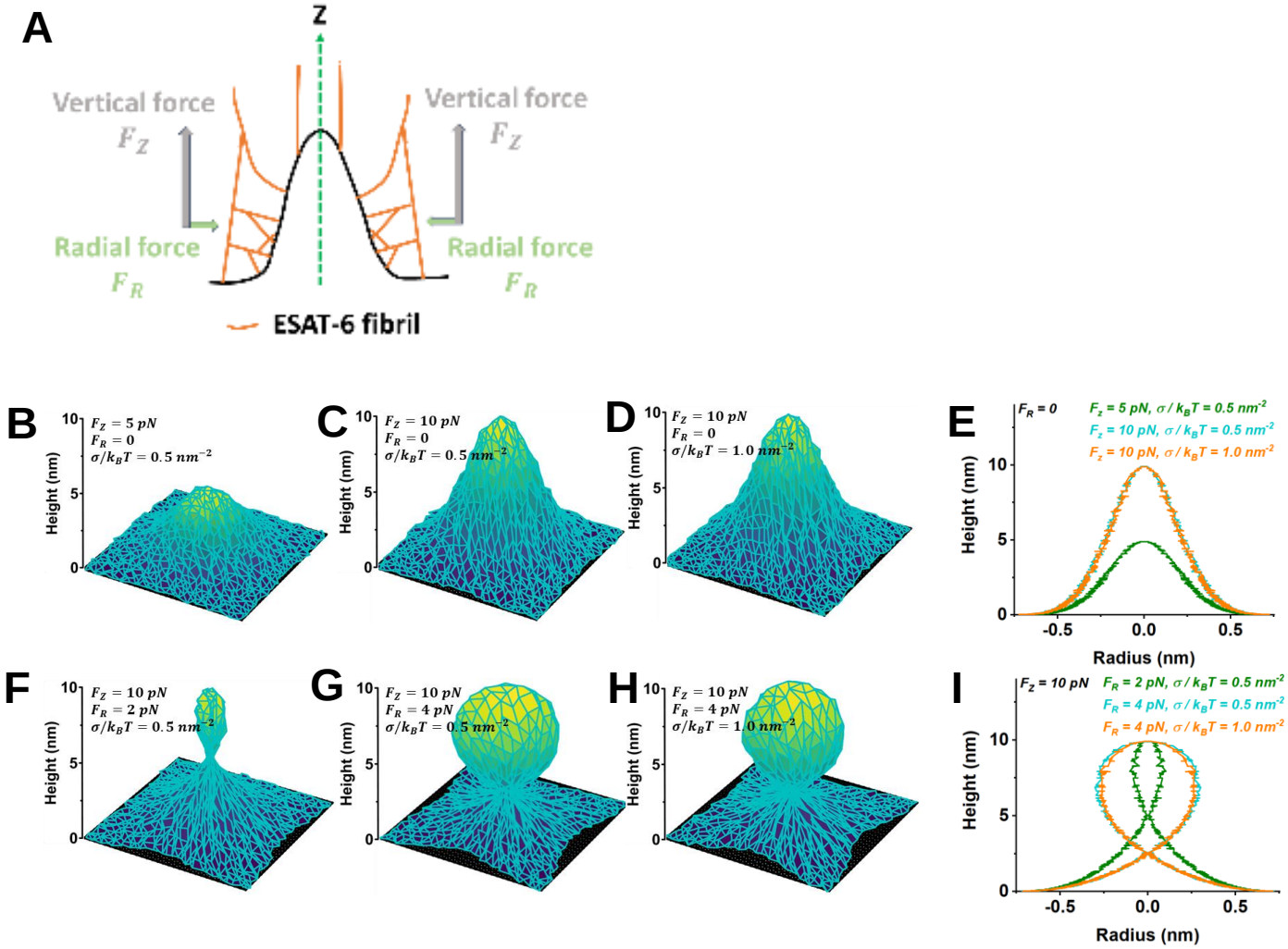
A
z
Vertical force
$F_Z$
Vertical force
$F_Z$
Radial force
$F_R$
Radial force
$F_R$
ESAT-6 fibril
B
$F_Z = 5\ pN$
$F_R = 0$
$\sigma/k_BT = 0.5\ nm^{-2}$
C
$F_Z = 10\ pN$
$F_R = 0$
$\sigma/k_BT = 0.5\ nm^{-2}$
D
$F_Z = 10\ pN$
$F_R = 0$
$\sigma/k_BT = 1.0\ nm^{-2}$
E
$F_R = 0$
$F_z = 5\ pN,\ \sigma/k_BT = 0.5\ nm^{-2}$
$F_z = 10\ pN,\ \sigma/k_BT = 0.5\ nm^{-2}$
$F_z = 10\ pN,\ \sigma/k_BT = 1.0\ nm^{-2}$
Height (nm)
Radius (nm)
F
$F_Z = 10\ pN$
$F_R = 2\ pN$
$\sigma/k_BT = 0.5\ nm^{-2}$
G
$F_Z = 10\ pN$
$F_R = 4\ pN$
$\sigma/k_BT = 0.5\ nm^{-2}$
H
$F_Z = 10\ pN$
$F_R = 4\ pN$
$\sigma/k_BT = 1.0\ nm^{-2}$
I
$F_Z = 10\ pN$
$F_R = 2\ pN,\ \sigma/k_BT = 0.5\ nm^{-2}$
$F_R = 4\ pN,\ \sigma/k_BT = 0.5\ nm^{-2}$
$F_R = 4\ pN,\ \sigma/k_BT = 1.0\ nm^{-2}$
Height (nm)
Radius (nm)

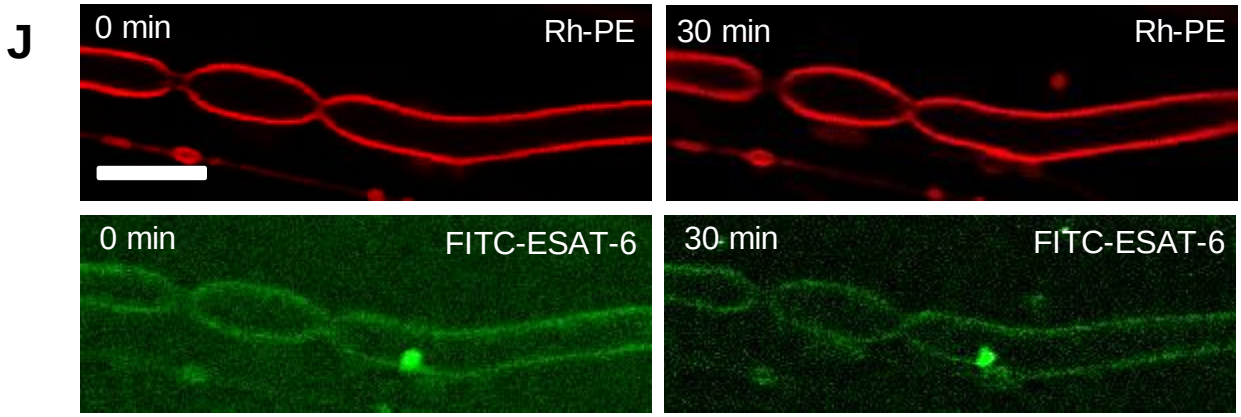
J
0 min
Rh-PE
30 min
Rh-PE
0 min
FITC-ESAT-6
30 min
FITC-ESAT-6

**Figure 4. ESAT-6 polymerization forces induce fission. a,** schematic showing the projections of radial and tangential forces generated by ESAT-6 polymerization. **b,c** A tubular bud emerges with the application of lateral force, $F_Z$, while the radial force $F_R = 0$. The surface tension $\sigma$ is kept at $0.5k_BT$. **d,** when an elevated surface tension ($\sigma = 1.0k_BT$) is applied, there are no significant changes in the shape of the tubular bud, even with forces $F_Z = 10\,pN$ and $F_R = 0$. **e,** Two-dimensional representation of the bud growth process depicted in **b-c. f,g** The radial force introduction results in a more spherical bud shape, with a connecting neck forming between the bud and the membrane. This effect is highlighted under a constant lateral force $F_Z = 10\,pN$. **h,** even with an elevated surface tension ($\sigma = 1.0k_BT$), the shape of the spherical bud remains relatively unchanged when subjected to forces $F_Z = 10\,pN$ and $F_R = 4\,pN$. **i,** Two-dimensional representation of radially influenced bud shape shown in **f-h. j,** Time-lapse confocal imaging of free-floating membrane tubes composed of phagosomal membrane composition labeled with 0.1% Rh-PE (red) and 5μM FITC-ESAT-6 (green). Representative image from three independent biological replicates.

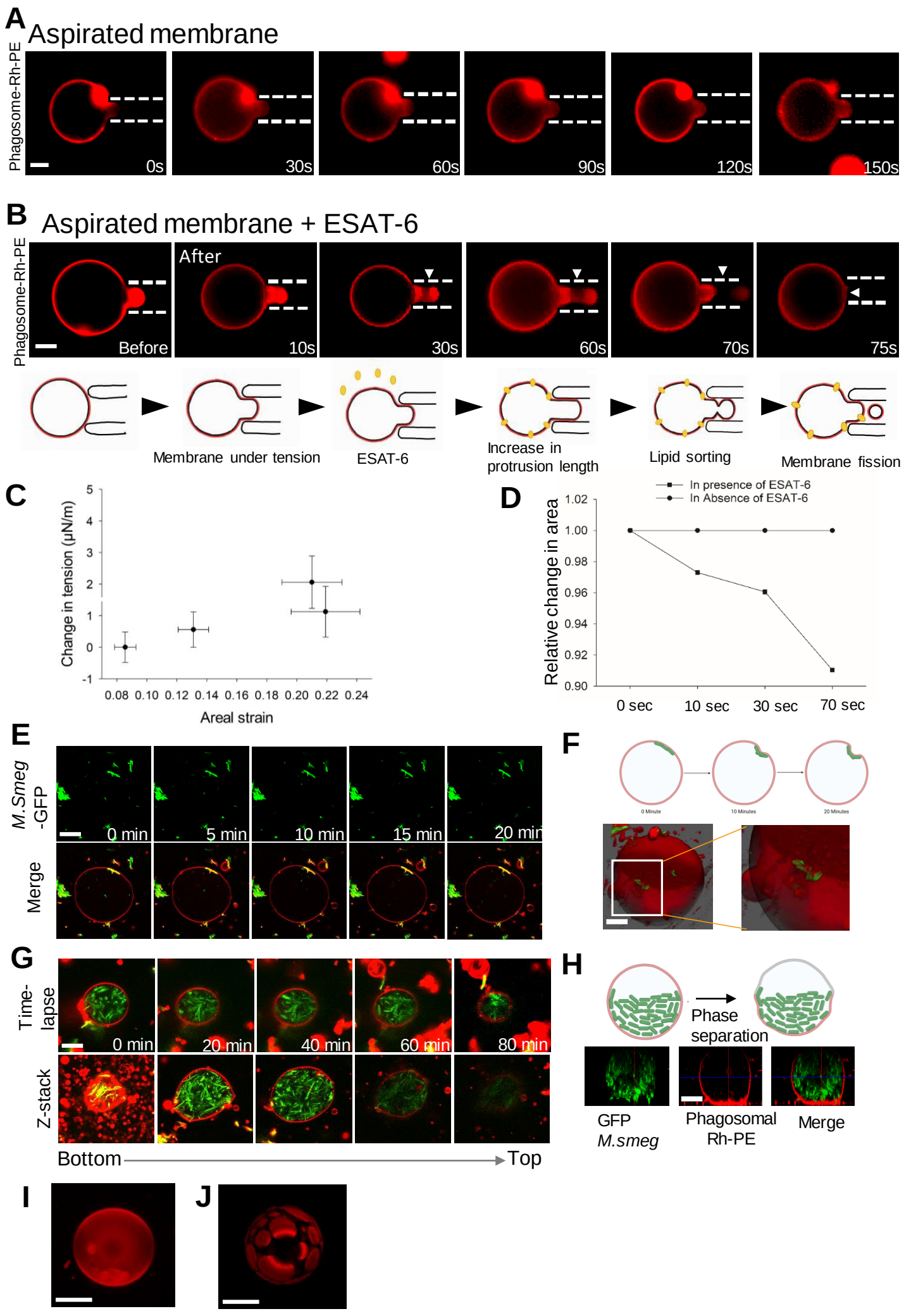
A
Aspirated membrane
Phagosome-Rh-PE
0s
30s
60s
90s
120s
150s
B
Aspirated membrane + ESAT-6
Phagosome-Rh-PE
Before
After
10s
30s
60s
70s
75s
Membrane under tension
ESAT-6
Increase in protrusion length
Lipid sorting
Membrane fission
C
Change in tension (μN/m)
Areal strain
D
In presence of ESAT-6
In Absence of ESAT-6
Relative change in area
0 sec
10 sec
30 sec
70 sec
E
M.Smeg -GFP
Merge
0 min
5 min
10 min
15 min
20 min
F
0 Minute
10 Minutes
20 Minutes
G
Time-lapse
Z-stack
0 min
20 min
40 min
60 min
80 min
Bottom
Top
H
Phase separation
GFP M.smeg
Phagosomal Rh-PE
Merge
I
J

938 **Figure 5. Phagosomal membrane vesiculation proceeds through local**
939 **modulation of curvature, lipid segregation and an increase in areal strain. a,**
940 Time-lapse fluorescence imaging of GUVs labeled with 0.1% Rh-PE (red) aspirated
941 with 50pa force and monitored over 150 seconds. **b,** Time-lapse fluorescence imaging
942 of GUVs labeled with 0.1% Rh-PE (red) aspirated with 50pa force followed by the
943 addition of unlabelled ESAT-6 and monitored over 75 seconds Scale bar, 5μm. **a&b**
944 Images are the representative of three independent experiments. **c,** Areal strain vs
945 change in tension plot from **b. d,** Relative change in membrane area plot from **a,b. e,**
946 Time-lapse confocal imaging of GUVs labeled with 0.1% Rh-PE (red) and immobilized
947 using 0.03% PEG-Biotin encapsulated with live *M.smegmatis* (green). Scale bar, 5μm.
948 Images are the representative of three independent experiments. **f,** schematic and 3D
949 projection of the mycobacteria-mediated curvature change from **e. g,** Time-lapse
950 confocal imaging and z-stack of GUVs labeled with 0.1% Rh-PE (red) and immobilized
951 using 0.03% PEG-Biotin encapsulated with the higher load of live *M.smegmatis*
952 (green). Scale bar, 5μm. Images are the representative of three independent
953 experiments. **h,** schematic and z-stack projection of the mycobacteria-induced
954 membrane phase separation of the membrane from **g.** Z-stack projection of **i,**
955 phagosomal membrane (Scale bar 10μm), and **j,** phase separation induced by the
956 lipid mixing of the phagosomal membrane and the mycobacterial cell envelope at 1:1
957 ratio (Scale bar 5μm) and labeled with 0.1% Rh-PE.
958

A

PBS

ESAT-6 5μM

ESAT-6 20μM

12 hour

24 hour

36 hour

Propidium iodide

Annexin-V

Necrotic

Late Apoptosis

Early Apoiptotic

Viable

B

Inset

Inset

C

500nm

**Figure 6. ESAT-6 induced apoptosis and cell death in a concentration and time-dependent manner. a,** Apoptosis was detected by flow cytometry in macrophage cells after stimulation with ESAT-6 (varying concentration) at different time points. Lower left (double negative), live cells; lower right (annexin V positive, PI-negative), early apoptosis; upper right (double positive), late apoptosis; upper left (annexin V negative, PI-positive), necrosis. Transmission electron micrographs capturing **b,** normal cell, and apoptotic cells are highlighted in the inset. **c,** elongated cells with ruptured membranes shown through white arrows. All the cells were treated with 20μM ESAT-6 followed by incubation for 24 hours. These are the representative images from three independent experiments.

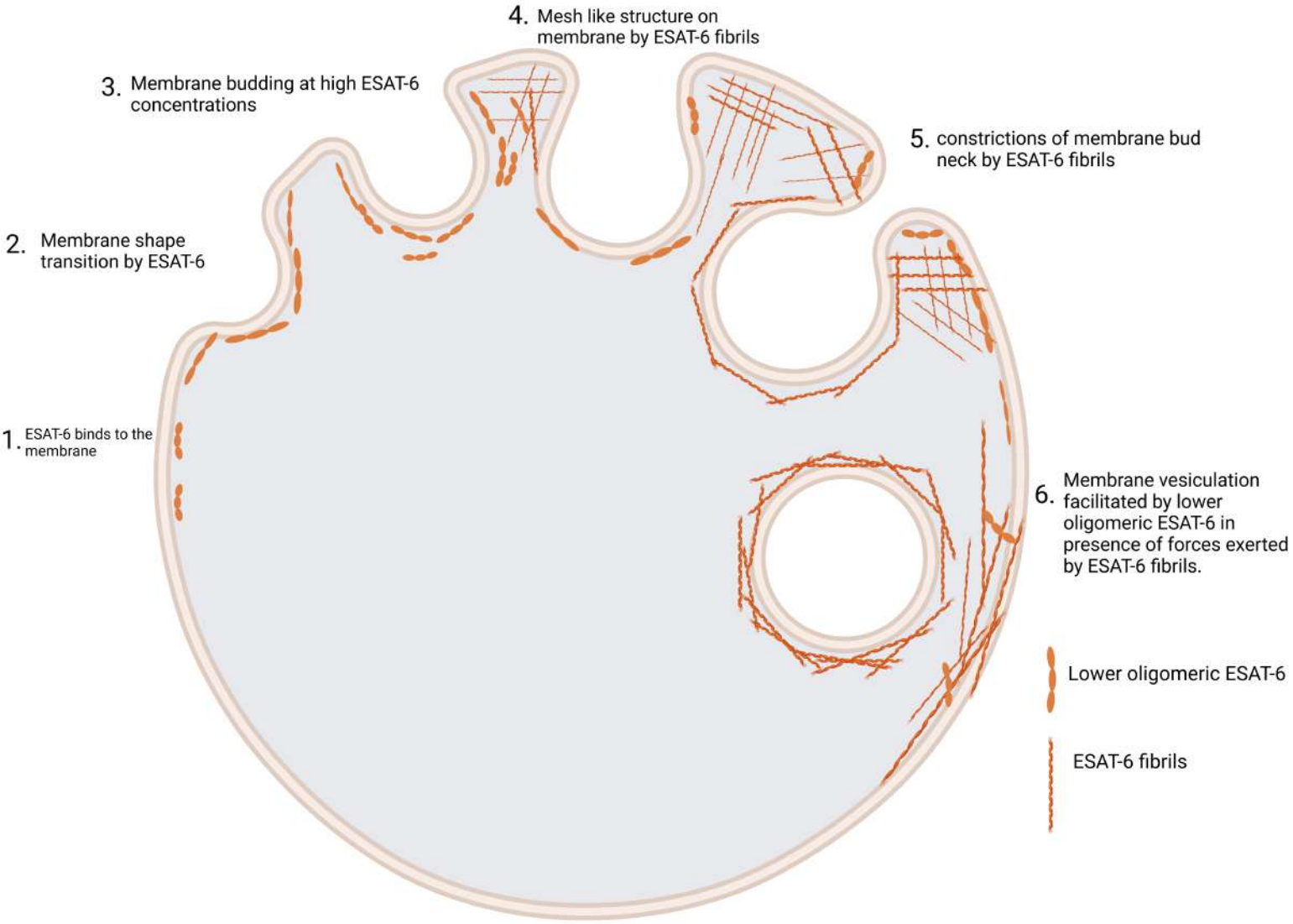
4. Mesh like structure on membrane by ESAT-6 fibrils
3. Membrane budding at high ESAT-6 concentrations
5. constrictions of membrane bud neck by ESAT-6 fibrils
2. Membrane shape transition by ESAT-6
1. ESAT-6 binds to the membrane
6. Membrane vesiculation facilitated by lower oligomeric ESAT-6 in presence of forces exerted by ESAT-6 fibrils.
Lower oligomeric ESAT-6
ESAT-6 fibrils

1008 **Figure 7. Schematic representation of the proposed mechanism of the ESAT-6**
1009 **fibril-mediated phagosomal deformation.**
1010
1011
1012

1013 REFERENCES-
1014


1015 1. Bussi, C. and M.G. Gutierrez, *Mycobacterium tuberculosis infection of host cells in*
1016 *space and time.* FEMS microbiology reviews, 2019. **43**(4): p. 341-361.
1017 2. Gröschel, M.I., et al., *ESX secretion systems: mycobacterial evolution to counter host*
1018 *immunity.* Nature Reviews Microbiology, 2016. **14**(11): p. 677-691.
1019 3. Renshaw, P.S., et al., *Structure and function of the complex formed by the tuberculosis*
1020 *virulence factors CFP-10 and ESAT-6.* The EMBO journal, 2005. **24**(14): p. 2491-2498.
1021 4. De Jonge, M.I., et al., *ESAT-6 from Mycobacterium tuberculosis dissociates from its*
1022 *putative chaperone CFP-10 under acidic conditions and exhibits membrane-lysing*
1023 *activity.* Journal of bacteriology, 2007. **189**(16): p. 6028-6034.
1024 5. Smith, J., et al., *Evidence for pore formation in host cell membranes by ESX-1-secreted*
1025 *ESAT-6 and its role in Mycobacterium marinum escape from the vacuole.* Infection and
1026 immunity, 2008. **76**(12): p. 5478-5487.
1027 6. van der Wel, N., et al., *M. tuberculosis and M. leprae translocate from the*
1028 *phagolysosome to the cytosol in myeloid cells.* Cell, 2007. **129**(7): p. 1287-1298.
1029 7. Houben, D., et al., *ESX-1-mediated translocation to the cytosol controls virulence of*
1030 *mycobacteria.* Cellular microbiology, 2012. **14**(8): p. 1287-1298.
1031 8. Simeone, R., et al., *Phagosomal rupture by Mycobacterium tuberculosis results in*
1032 *toxicity and host cell death.* PLoS pathogens, 2012. **8**(2): p. e1002507.
1033 9. De Leon, J., et al., *Mycobacterium tuberculosis ESAT-6 exhibits a unique membrane-*
1034 *interacting activity that is not found in its ortholog from non-pathogenic*
1035 *Mycobacterium smegmatis.* Journal of Biological Chemistry, 2012. **287**(53): p. 44184-
1036 44191.
1037 10. Ma, Y., V. Keil, and J. Sun, *Characterization of Mycobacterium tuberculosis EsxA*
1038 *membrane insertion: roles of N-and C-terminal flexible arms and central helix-turn-*
1039 *helix motif.* Journal of Biological Chemistry, 2015. **290**(11): p. 7314-7322.
1040 11. Conrad, W.H., et al., *Mycobacterial ESX-1 secretion system mediates host cell lysis*
1041 *through bacterium contact-dependent gross membrane disruptions.* Proceedings of
1042 the National Academy of Sciences, 2017. **114**(6): p. 1371-1376.
1043 12. Augenstreich, J., et al., *ESX-1 and phthiocerol dimycocerosates of Mycobacterium*
1044 *tuberculosis act in concert to cause phagosomal rupture and host cell apoptosis.*
1045 Cellular microbiology, 2017. **19**(7): p. e12726.
1046 13. Osman, M.M., et al., *The C terminus of the mycobacterium ESX-1 secretion system*
1047 *substrate ESAT-6 is required for phagosomal membrane damage and virulence.*
1048 Proceedings of the National Academy of Sciences, 2022. **119**(11): p. e2122161119.
1049 14. Barczak, A.K., et al., *Systematic, multiparametric analysis of Mycobacterium*
1050 *tuberculosis intracellular infection offers insight into coordinated virulence.* PLoS
1051 pathogens, 2017. **13**(5): p. e1006363.
1052 15. Astarie-Dequeker, C., et al., *Phthiocerol dimycocerosates of M. tuberculosis participate*
1053 *in macrophage invasion by inducing changes in the organization of plasma membrane*
1054 *lipids.* PLoS pathogens, 2009. **5**(2): p. e1000289.
1055 16. Lienard, J., et al., *The Mycobacterium marinum ESX-1 system mediates phagosomal*
1056 *permeabilization and type I interferon production via separable mechanisms.*
1057 Proceedings of the National Academy of Sciences, 2020. **117**(2): p. 1160-1166.

1058 17. Kennedy, G.M., et al., *A novel ESX-1 locus reveals that surface-associated ESX-1*
1059 *substrates mediate virulence in Mycobacterium marinum.* Journal of bacteriology,
1060 2014. **196**(10): p. 1877-1888.
1061 18. Raffetseder, J., et al., *Retention of EsxA in the capsule-like layer of Mycobacterium*
1062 *tuberculosis is associated with cytotoxicity and is counteracted by lung surfactant.*
1063 Infection and immunity, 2019. **87**(3): p. 10-1128.
1064 19. Ingólfsson, H.I., et al., *Computational lipidomics of the neuronal plasma membrane.*
1065 Biophysical journal, 2017. **113**(10): p. 2271-2280.
1066 20. Bates, T.A., et al., *ESAT-6 undergoes self-association at phagosomal pH and an ESAT-*
1067 *6 specific nanobody restricts M. tuberculosis growth in macrophages*. 2023, Cold
1068 Spring Harbor Laboratory.
1069 21. Bertin, A., et al., *Human ESCRT-III polymers assemble on positively curved membranes*
1070 *and induce helical membrane tube formation.* Nature communications, 2020. **11**(1): p.
1071 2663.
1072 22. Mim, C., et al., *Structural basis of membrane bending by the N-BAR protein endophilin.*
1073 Cell, 2012. **149**(1): p. 137-145.
1074 23. Saleem, M., et al., *A balance between membrane elasticity and polymerization energy*
1075 *sets the shape of spherical clathrin coats.* Nature communications, 2015. **6**(1): p. 6249.
1076 24. Muraoka, T., et al., *A synthetic ion channel with anisotropic ligand response.* Nature
1077 communications, 2020. **11**(1): p. 2924.
1078 25. Dijkman, P.M., et al., *Conformational dynamics of a G protein–coupled receptor helix*
1079 *8 in lipid membranes.* Science advances, 2020. **6**(33): p. eaav8207.
1080 26. Hsu, T., et al., *The primary mechanism of attenuation of bacillus Calmette–Guerin is a*
1081 *loss of secreted lytic function required for invasion of lung interstitial tissue.*
1082 Proceedings of the National Academy of Sciences, 2003. **100**(21): p. 12420-12425.
1083 27. Gotthardt, D., et al., *High-resolution dissection of phagosome maturation reveals*
1084 *distinct membrane trafficking phases.* Molecular biology of the cell, 2002. **13**(10): p.
1085 3508-3520.
1086 28. Colom, A., et al., *A fluorescent membrane tension probe.* Nature chemistry, 2018.
1087 **10**(11): p. 1118-1125.
1088 29. Mercier, V., et al., *Endosomal membrane tension regulates ESCRT-III-dependent intra-*
1089 *lumenal vesicle formation.* Nature cell biology, 2020. **22**(8): p. 947-959.
1090 30. Brockman, H., *Lipid monolayers: why use half a membrane to characterize protein-*
1091 *membrane interactions?* Current opinion in structural biology, 1999. **9**(4): p. 438-443.
1092 31. Yang, S.-T., V. Kiessling, and L.K. Tamm, *Line tension at lipid phase boundaries as*
1093 *driving force for HIV fusion peptide-mediated fusion.* Nature communications, 2016.
1094 **7**(1): p. 11401.
1095 32. Nitenberg, M., et al., *The potent effect of mycolactone on lipid membranes.* PLoS
1096 pathogens, 2018. **14**(1): p. e1006814.
1097 33. Marsh, D., *Elastic curvature constants of lipid monolayers and bilayers.* Chemistry and
1098 physics of lipids, 2006. **144**(2): p. 146-159.
1099 34. Courtemanche, N., et al., *Tension modulates actin filament polymerization mediated*
1100 *by formin and profilin.* 2013. **110**(24): p. 9752-9757.
1101 35. Yu, M., et al., *mDia1 senses both force and torque during F-actin filament*
1102 *polymerization.* 2017. **8**(1): p. 1650.
1103 36. Yu, M., et al., *Effects of mechanical stimuli on profilin-and formin-mediated actin*
1104 *polymerization.* 2018. **18**(8): p. 5239-5247.

37. Lipowsky, R., *Remodeling of membrane shape and topology by curvature elasticity and membrane tension.* Advanced Biology, 2022. **6**(1): p. 2101020.
38. Berezin, M.Y. and S. Achilefu, *Fluorescence lifetime measurements and biological imaging.* Chemical reviews, 2010. **110**(5): p. 2641-2684.
39. Wang, L., et al., *Bacterial inclusion bodies contain amyloid-like structure.* PLoS biology, 2008. **6**(8): p. e195.
40. McGlinchey, R.P., et al., *The N terminus of α-synuclein dictates fibril formation.* 2021. **118**(35): p. e2023487118.
41. Despres, C., et al., *Identification of the Tau phosphorylation pattern that drives its aggregation.* 2017. **114**(34): p. 9080-9085.
42. Tiwari, A., et al., *Interplay of lipid head group and packing defects in driving amyloid-beta–mediated myelin-like model membrane deformation.* Journal of Biological Chemistry, 2023. **299**(5).
43. Bates, T.A., et al., *ESAT-6 undergoes self-association at phagosomal pH and an ESAT-6-specific nanobody restricts M. tuberculosis growth in macrophages.* 2024. **12**: p. RP91930.
44. Rose, K., et al., *Tau fibrils induce nanoscale membrane damage and nucleate cytosolic tau at lysosomes.* 2024. **121**(22): p. e2315690121.
45. Shin, W., et al., *Molecular mechanics underlying flat-to-round membrane budding in live secretory cells.* Nature Communications, 2022. **13**(1): p. 3697.
46. Zhang, T., et al., *On the modeling of endocytosis in yeast.* Biophysical journal, 2015. **108**(3): p. 508-519.
47. Helfrich, W., *Elastic properties of lipid bilayers: theory and possible experiments.* Zeitschrift für Naturforschung c, 1973. **28**(11-12): p. 693-703.
48. Kozlovsky, Y. and M.M. Kozlov, *Membrane fission: model for intermediate structures.* Biophysical journal, 2003. **85**(1): p. 85-96.
49. Kozlov, M.M., *Fission of biological membranes: interplay between dynamin and lipids.* Traffic, 2001. **2**(1): p. 51-65.
50. Alimohamadi, H. and P. Rangamani, *Modeling membrane curvature generation due to membrane–protein interactions.* Biomolecules, 2018. **8**(4): p. 120.
51. Hassinger, J., et al., *Design principles for robust vesiculation in clathrin-mediated endocytosis.* Biophysical Journal, 2017. **112**(3): p. 310a.
52. Rangamani, P., K.K. Mandadap, and G. Oster, *Protein-induced membrane curvature alters local membrane tension.* Biophysical journal, 2014. **107**(3): p. 751-762.
53. Fošnarič, M., et al., *Theoretical study of vesicle shapes driven by coupling curved proteins and active cytoskeletal forces.* Soft Matter, 2019. **15**(26): p. 5319-5330.
54. Baumgart, T., et al., *Large-scale fluid/fluid phase separation of proteins and lipids in giant plasma membrane vesicles.* Proceedings of the National Academy of Sciences, 2007. **104**(9): p. 3165-3170.
55. Baumgart, T., et al., *Fluorescence probe partitioning between Lo/Ld phases in lipid membranes.* Biochimica et Biophysica Acta (BBA)-Biomembranes, 2007. **1768**(9): p. 2182-2194.
56. Shi, Z. and T. Baumgart, *Membrane tension and peripheral protein density mediate membrane shape transitions.* Nature communications, 2015. **6**(1): p. 5974.
57. Lerner, T.R., et al., *Phthiocerol dimycocerosates promote access to the cytosol and intracellular burden of Mycobacterium tuberculosis in lymphatic endothelial cells.* BMC biology, 2018. **16**(1): p. 1-13.

1152 58. Behura, A., et al., *ESAT-6 modulates Calcimycin-induced autophagy through*
1153 *microRNA-30a in mycobacteria infected macrophages.* Journal of Infection, 2019.
1154 **79**(2): p. 139-152.
1155 59. Lin, J., et al., *Early secreted antigenic target of 6-kDa of Mycobacterium tuberculosis*
1156 *promotes caspase-9/caspase-3-mediated apoptosis in macrophages.* Molecular and
1157 Cellular Biochemistry, 2019. **457**: p. 179-189.
1158 60. Simeone, R., et al., *Breaching the phagosome, the case of the tuberculosis agent.*
1159 Cellular Microbiology, 2021. **23**(7): p. e13344.
1160 61. McMahon, H.T. and E. Boucrot, *Membrane curvature at a glance.* Journal of cell
1161 science, 2015. **128**(6): p. 1065-1070.
1162 62. Tak, U., T. Dokland, and M. Niederweis, *Pore-forming Esx proteins mediate toxin*
1163 *secretion by Mycobacterium tuberculosis.* Nature Communications, 2021. **12**(1): p.
1164 394.
1165 63. Mulvihill, E., et al., *Mechanism of membrane pore formation by human gasdermin-D.*
1166 2018. **37**(14): p. e98321.
1167 64. Yu, X., et al., *Cryo-EM structures of perforin-2 in isolation and assembled on a*
1168 *membrane suggest a mechanism for pore formation.* 2022. **41**(23): p. e111857.
1169 65. Sborgi, L., et al., *GSDMD membrane pore formation constitutes the mechanism of*
1170 *pyroptotic cell death.* 2016. **35**(16): p. 1766-1778.
1171 66. Sheetz, M.P. and S.J. Singer, *Biological membranes as bilayer couples. A molecular*
1172 *mechanism of drug-erythrocyte interactions.* Proceedings of the National Academy of
1173 Sciences, 1974. **71**(11): p. 4457-4461.
1174 67. Roux, A., *Common principles of surface deformation in biology.* Faraday Discussions,
1175 2021. **232**: p. 347-357.
1176 68. Campelo, F., H.T. McMahon, and M.M. Kozlov, *The hydrophobic insertion mechanism*
1177 *of membrane curvature generation by proteins.* Biophysical journal, 2008. **95**(5): p.
1178 2325-2339.
1179 69. Stachowiak, J.C., et al., *Membrane bending by protein–protein crowding.* Nature cell
1180 biology, 2012. **14**(9): p. 944-949.
1181 70. Simunovic, M., et al., *When physics takes over: BAR proteins and membrane curvature.*
1182 Trends in cell biology, 2015. **25**(12): p. 780-792.
1183 71. Ford, M.G.J., et al., *Curvature of clathrin-coated pits driven by epsin.* Nature, 2002.
1184 **419**(6905): p. 361-366.
1185 72. Martens, S., M.M. Kozlov, and H.T. McMahon, *How synaptotagmin promotes*
1186 *membrane fusion.* Science, 2007. **316**(5828): p. 1205-1208.
1187 73. Peter, B.J., et al., *BAR domains as sensors of membrane curvature: the amphiphysin*
1188 *BAR structure.* Science, 2004. **303**(5657): p. 495-9.
1189 74. Lancaster, C.E., et al., *Phagosome resolution regenerates lysosomes and maintains the*
1190 *degradative capacity in phagocytes.* Journal of Cell Biology, 2021. **220**(9): p.
1191 e202005072.
1192 75. Engel, M.F.M., et al., *Membrane damage by human islet amyloid polypeptide through*
1193 *fibril growth at the membrane.* Proceedings of the National Academy of Sciences,
1194 2008. **105**(16): p. 6033-6038.
1195 76. Milanesi, L., et al., *Direct three-dimensional visualization of membrane disruption by*
1196 *amyloid fibrils.* Proceedings of the National Academy of Sciences, 2012. **109**(50): p.
1197 20455-20460.

77. Chiaruttini, N., et al., *Relaxation of loaded ESCRT-III spiral springs drives membrane deformation.* Cell, 2015. **163**(4): p. 866-879.
78. Dar, S., S.C. Kamerkar, and T.J. Pucadyil, *A high-throughput platform for real-time analysis of membrane fission reactions reveals dynamin function.* Nature cell biology, 2015. **17**(12): p. 1588-1596.
79. Roux, A., et al., *Role of curvature and phase transition in lipid sorting and fission of membrane tubules.* The EMBO journal, 2005. **24**(8): p. 1537-1545.
80. Sorre, B., et al., *Curvature-driven lipid sorting needs proximity to a demixing point and is aided by proteins.* Proceedings of the National Academy of Sciences, 2009. **106**(14): p. 5622-5626.
81. Aguilo, J.I., et al., *ESX-1-induced apoptosis is involved in cell-to-cell spread of M ycobacterium tuberculosis.* Cellular microbiology, 2013. **15**(12): p. 1994-2005.
82. Davis, J.M. and L. Ramakrishnan, *The role of the granuloma in expansion and dissemination of early tuberculous infection.* Cell, 2009. **136**(1): p. 37-49.
83. Schaible, U.E., et al., *Apoptosis facilitates antigen presentation to T lymphocytes through MHC-I and CD1 in tuberculosis.* Nature medicine, 2003. **9**(8): p. 1039-1046.
84. Blomgran, R., et al., *Mycobacterium tuberculosis inhibits neutrophil apoptosis, leading to delayed activation of naive CD4 T cells.* Cell host & microbe, 2012. **11**(1): p. 81-90.
85. Aguiló, N., et al., *ESX-1-induced apoptosis during mycobacterial infection: to be or not to be, that is the question.* Frontiers in cellular and infection microbiology, 2013. **3**: p. 88.
86. Choudhary, V., et al., *A conserved family of proteins facilitates nascent lipid droplet budding from the ER.* Journal of Cell Biology, 2015. **211**(2): p. 261-271.
87. Rezwan, M., et al., *Breaking down the wall: fractionation of mycobacteria.* Journal of microbiological methods, 2007. **68**(1): p. 32-39.
88. Reis, A., et al., *A comparison of five lipid extraction solvent systems for lipidomic studies of human LDL [S].* Journal of lipid research, 2013. **54**(7): p. 1812-1824.

## Acknowledgements

We thank Thierry Soldati for critical comments on the manuscript. We thank Rohan Dhiman for the kind gift of the ESAT-6 and CFP-10 plasmid and GFP-*M.smegmatis* strain. We thank Subhasis Chattopadhyay for his assistance with the Flow cytometry. We acknowledge all the members of M.S. lab for critical reading of the manuscript. MS greatfully acknowledge the DBT-Wellcome Trust India Alliance (Grant-IA/I/20/2/505212), Department of Atomic Energy for financial support for intramural support and SERB, India for National postdoctoral Fellowship to MN (PDF/2022/001807).